University of California, San Diego UCSD-CER-05-01

Radiation-Hydrodynamic Analysis of Ti-Doped SiO_2 Aerogel Exposed to 4-ns Laser Irradiation

M. S. Tillack, J. O'Shay, E. S. Simpson,
C. A. Back and H. A. Scott

10 January 2005

Center for Energy Research
University of California, San Diego
9500 Gilman Drive
La Jolla, CA 92093-0420

Radiation-Hydrodynamic Analysis of Ti-Doped SiO_2 Aerogel Exposed to 4-ns Laser Irradiation

10 January 2005

M. S. Tillack, J. O'Shay,[1] E. S. Simpson
UC San Diego
Mechanical and Aerospace Engineering Department
[1] Electrical and Computer Engineering Department

C. A. Back and H. A. Scott
Lawrence Livermore National Laboratory

Abstract

We used the Hyades [1] and Helios [2] radiation-hydrodynamic simulation tools to explore the response of low-density SiO_2 aerogel carriers doped with trace amounts of Ti and subjected to high-energy pulsed laser irradiation. At sufficiently low density, these targets are expected to respond to laser irradiation more uniformly as compared with solid targets, and therefore provide a better platform upon which to perform measurements of the properties of hot dense matter. In this report we describe our initial modeling results for several cases of interest, with laser intensities in the range of 4.9×10^{12} to 3.7×10^{14} W/cm^2, SiO_2 densities in the range of 2 to 8 mg/cm^3 and Ti doping in the range of 0 to 6%.

Table of Contents

List of Figures

1. Background

1.1 Problem description

A new project was initiated at LLNL during 2004 to develop absolute spectroscopic diagnostics. The research involves experiments and theory aimed at investigating atomic kinetics of highly ionized plasmas. The experiments use low-density SiO_2 aerogel foams that permit measurement of the temporal evolution of the K and L-shell emission of highly-ionized species using new absolute spectroscopic diagnostics. The data are expected to be sufficiently accurate to enable the creation of benchmarks, which can be used to refine and potentially validate the non-local thermodynamic equilibrium (NLTE) models used at LLNL and other research laboratories. In particular, recombination processes with electron densities in the range of 10^{19} to 10^{22} cm^{-3} for mid-Z elements will be addressed in experiments where an independent measure of the electron temperature is made for a sample with a well-known initial mass density. The experiments will provide *temporally-resolved absolute* measurements of the emission over a spectral range of 200 to 1000 eV.

This project addresses long-standing discrepancies in the study of laser-produced plasmas. Discrepancies between data and calculations of laser-produced plasmas in recombination have been evident since the 1980's. [3] One example of a large discrepancy is in predictions of the x-ray source duration for times greater than the laser pulse duration. The problem might be in the hydrodynamics; however, there are indications that non-LTE atomic kinetics may be the dominant cause of discrepancies. Recent international workshops on non-LTE kinetics have uncovered major disagreements in predictions from 16 different codes for plasma temperature and density cases that were chosen for relevance to laboratory plasma studies. [4] The inability to accurately model x-ray laser recombination schemes is a prominent illustration that the models are incomplete.

In order to help interpret the results of experiments, we have begun to model low-density doped aerogels using available numerical models. Radiation-hydrodynamic simulations were performed using Hydades [1] and Helios [2] over a range of parameters for laser intensities from 4.9×10^{12} to 3.7×10^{14} W/cm^2. Different modeling options were explored, with a particular emphasis on radiation transport and atomic physics models, in order to determine their relative importance and the need for more sophisticated modeling in the future. All of the modeling results presented in this work assume local thermodynamic equilibrium (LTE).

1.2 Codes and modeling options

Models of the behavior of high-Z dense laser plasmas include one or more of the following three components in order to characterize the material responses:

(1) The basic hydrodynamics and energy transport. This includes laser absorption models, hydrodynamic models which utilize tabulated or computed equations of state for pressure and internal energy, and a radiation energy transport model. Radiation hydrodynamic codes often make simplifications for the radiation emission and transport, and may assume local thermodynamic equilibrium. Examples of radiation transport algorithms include flux-limited diffusion or multi-angle short characteristics.

(2) Equation of state and opacity data or models. EOS and opacity data are essential in order to provide an accurate prediction of plasma responses. They can be obtained from databases, such as Sesame, or generated internally by the software package. Opacity data may be spectrally resolved or spectrally averaged (*i.e.,* "gray").

(3) A time-dependent collisional radiative (CR) solver for non-LTE plasmas. CR models require data on the relevant atomic processes which influence the ionization, excitation and emission of atoms, including:
   - Collisional ionization, recombination, excitation, and deexcitation
   - Photoionization and stimulated recombination
   - Photoexcitation and stimulated emission
   - Spontaneous decay
   - Radiative recombination
   - Dielectronic recombination, autoionization, and electron capture.

   The codes solve rate equations for the evolution of the various atomic levels. For mid to high Z elements, the large number of trasitions usually requires some form of simplification, or "compression", of the data.

One of the codes we used for our plasma analysis is Hyades [1]. HYADES is a one-dimensional, three-temperature, Lagrangian hydrodynamics and energy transport code. The electron and ion components are treated separately in a fluid approximation and are loosely coupled to each other, each in thermodynamic equilibrium and described by Maxwell-Boltzmann statistics. Radiative energy transport is treated in a single-group (gray approximation) or in a multi-group prescription; in the former, the radiation is assumed Planckian, and the latter model allows for small departures from a pure Planckian. Hence, the multi-group method may be used to include some atomic shell effects and crude x-ray line effects. The radiation is coupled only to the electron fluid. The diffusion approximation is used for modeling all energy transport phenomena. The degree of ionization is determined by a Saha, Thomas-Fermi, LTE average-atom, time-dependent or steady-state nonLTE average-atom, or fully stripped models.

The thermodynamic and equation of state quantities are derived from realistic (Sesame or other theoretical models) tables, an in-line quotidian equation of state (QEOS), or an ideal gas model. Likewise, the tabular Rosseland mean and Planck mean opacities used in the gray radiation transport model are obtained from reasonable models. The hydrodynamic motion is treated in the Lagrangian formalism since the plasma may expand to cover a large spatial extent, as well as ranging over several orders of magnitude in density. In the Lagrangian prescription, the mesh moves with the material; that is, each elemental mass (zone) is conserved for all time. In contrast is the Eulerian prescription in which the mesh stays fixed and the material moves through it.

The other code we used in our analysis is Helios [2]. Helios is a 1-D radiation-hydrodynamics code developed by Prism Computational Sciences Inc. The hydrodynamic models are similar to Hyades. EOS and opacity data can be obtained from Sesame, but the default uses EOS and spectrally resolved opacity data obtained from the PROPACEOS code (PRism OPACity and Equation Of State code). PROPACEOS computes data for LTE plasmas or optically thin non-LTE plasmas. A full CR version of Helios is available, in which basic atomic data is supplied by the ATBASE suite of codes. In the work presented here, we have included only LTE cases.

1.3 Overview

The primary goal of this numerical study is to characterize the response of low-density Ti-doped aerogels irradiated in experiments at the Janus and Nike laser facilities. The set of parameters to be investigated is summarized in Table I. For all cases the laser source term remained the same: 248 nm light ramping up in 0.2 ns, flat top for 3.6 ns, followed by a 0.2 ns rampdown.

Table I. Experimental laser and target parameters

Case #	Description	Ti wt%	SiO_2 density (mg/cm^3)	laser intensity (TW/cm^2)
0	modeling base case	0	2	4.9
1	experimental base case	2	2	4.9
2	high Ti dopant case	**6**	2	4.9
3	high SiO_2 density case	2	**8**	4.9
4	thin target case	2	2	4.9
5	high laser intensity case	2	2	**370**
6	high intensity, high doping	**6**	2	**370**

Due to uncertainties in the validity of the numerical models in the codes and the sensitivity of the results to modeling assumptions, we first examined a "modeling base case" consisting of pure SiO_2. This is labeled "Case 0" in the table. In all other respects it is identical to the experimental base case. We explored the grid dependence, radiation transport model and the source of opacity data for Hyades, and compared the results with Helios.

After fully characterizing the modeling base case, we performed parametric variations by changing one parameter at a time. First, the Ti dopant level was increased from 0 to 6 wt%. After that, the target initial density was increased by a factor of 4. Based on our observations of strong laser absorption in this and the base case, we added a case with a thinner (0.5 mm) target in order to explore the effect of the optical depth with respect to the incident laser. Finally, the laser intensity was increased to 3.7×10^{14} W/cm^2.

Key parameters that we examined in the analysis included electron temperature, electron density, charge state and laser flux *vs*. time and zone. We are looking for the plasma to achieve a relatively uniform electron density during the laser pulse, and a relatively uniform temperature. This

should also lead to a relatively uniform average charge state in the plasma. Finally, we are interested to determine whether the incident laser is penetrating effectively into the underdense plasma, or if heating of the rear side of the target is dominated by conduction and/or radiation from the front (laser-facing) side.

2. Base Case Analysis

2.1 Base case results for pure SiO_2 at 4.9×10^{12} W/cm^2

2.1.1 Hyades base case results

In order to establish a clear, well-characterized reference case for the purpose of comparison, we first examined a simple target with pure SiO_2 (*i.e.,* no doping) at 2 mg/cm^2 density. The Hyades input file is listed in Appendix B1. This case, as with all the cases presented here, used a temporal profile consisting of a 0.2-ns linear ramp-up to full laser intensity, followed by a 3.6-ns flat-top and then a 0.2-ns ramp-down to zero. The flat-top intensity for the base case was 4.9×10^{12} W/cm^2. We chose to use a uniform grid, with no feathering near the illumination source, for three reasons: (1) this grid allowed us to perform the most direct side-by-side comparison of Hyades and Helios, (2) results are easier to interpret in a uniform grid (where the spatial coordinate and mass coordinate are simply related), and (3) these low-density targets do not exhibit sharp gradients as with fully-dense targets, and so we do not expect feathering to be necessary. The equation of state and opacity were derived from Sesame [5] data tables. For the Hyades base case, gray (spectrally averaged) opacities were used.

Figures 1 and 2 show the time histories of electron temperature and density in each Lagrangian zone. Excluding the outermost zone (which we show later to be an artifact of the grid), a peak temperature of ~130 eV is reached at the end of the pulse. The variation in temperature through the target is about a factor of two, with the minimum (located at the back side) of ~55 eV. The temperature gradient is relatively smooth from front to back. Figure 3 shows the spatial profile of electron temperature at 2.5 ns into the pulse; about 60% of the plasma has very uniform temperature (~55 eV), whereas the outermost 40% is more strongly heated.

Figure 4 shows the integrated laser intensity through the plasma, zone by zone, for the outermost half of the target. This parameter depicts the amount of laser light which reaches any given location in the target as a function of time. Clearly, the rear side of the target is not reached by the incident laser during the 4-ns pulse.

Inverse bremsstrahlung is the dominant mechanism for laser absorption in this underdense target. The absorption follows an exponential decay:

$$dI/dx = -\alpha I$$

where the absorption coefficient α is given by:

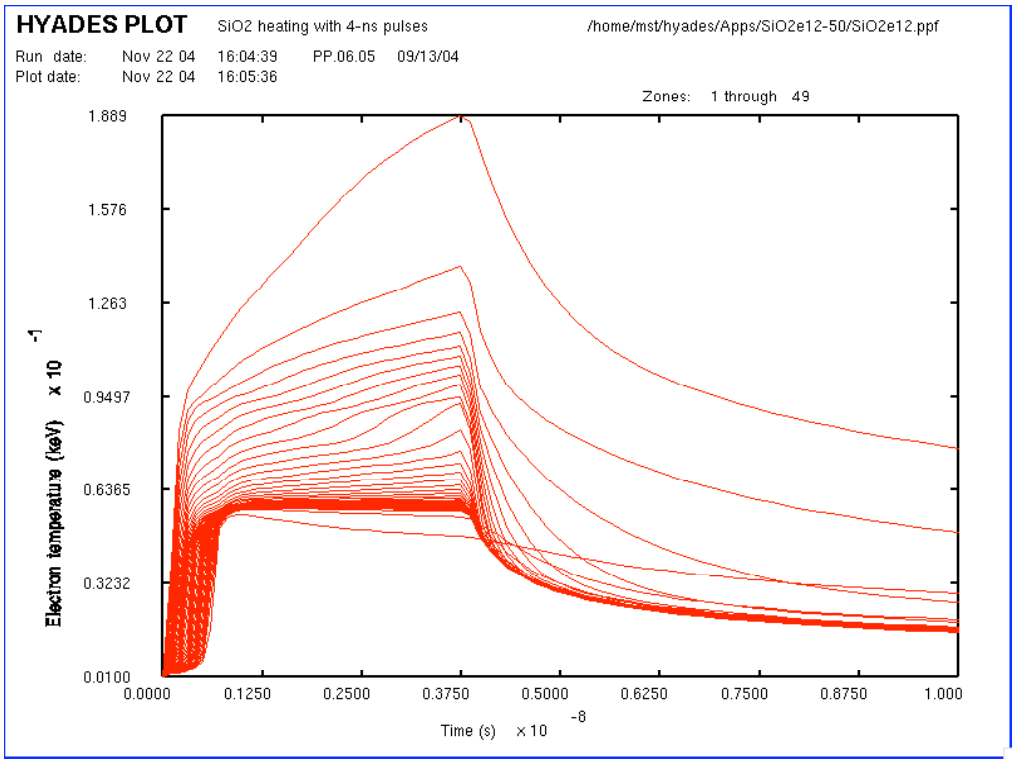

Figure 1. Electron temperature history at 50 equal-mass zones for the Hyades base case

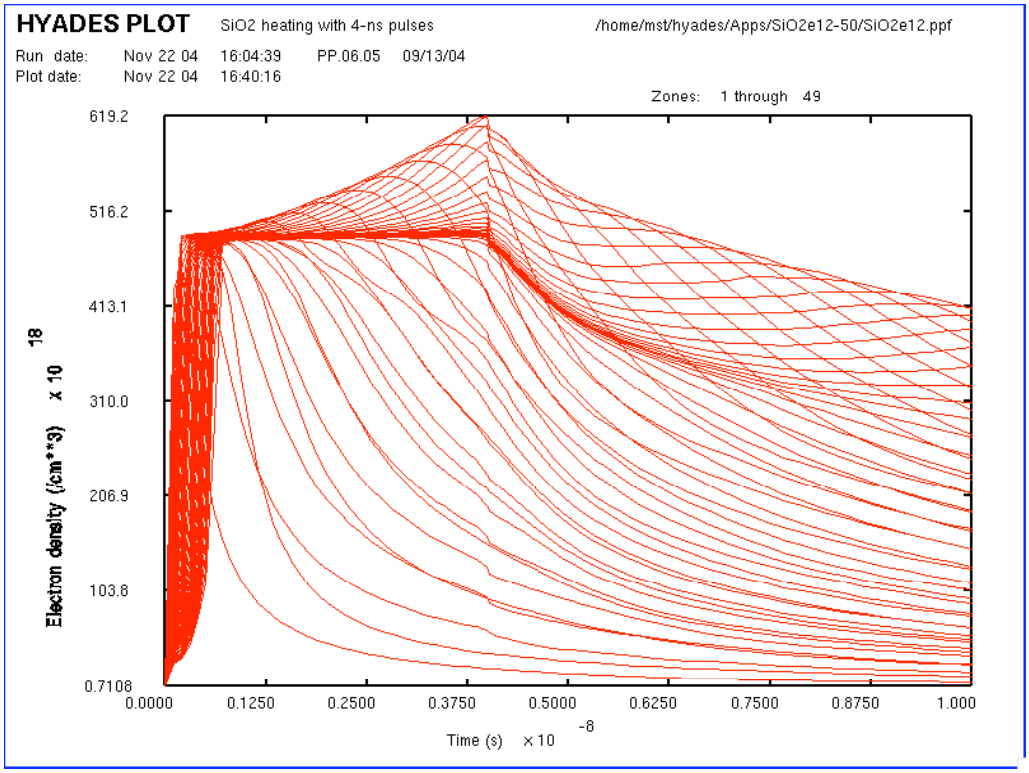

Figure 2. Electron density history at 50 equal-mass zones for the Hyades base case

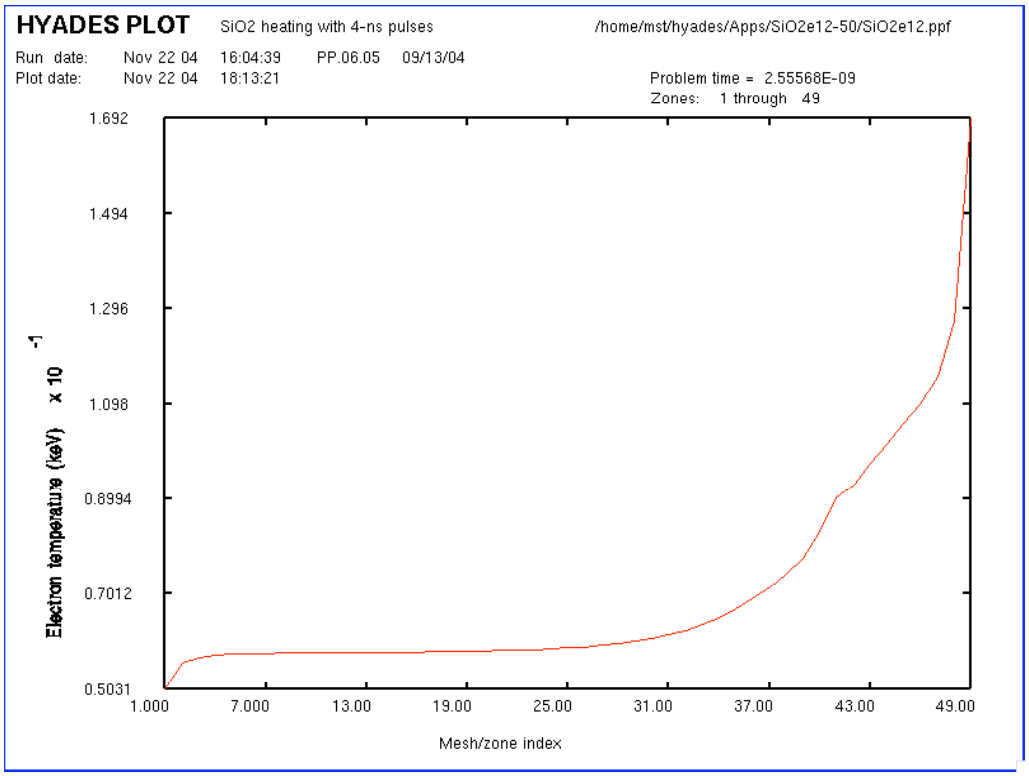

Figure 3. Electron temperature spatial profile at 2.5 ns for the Hyades base case

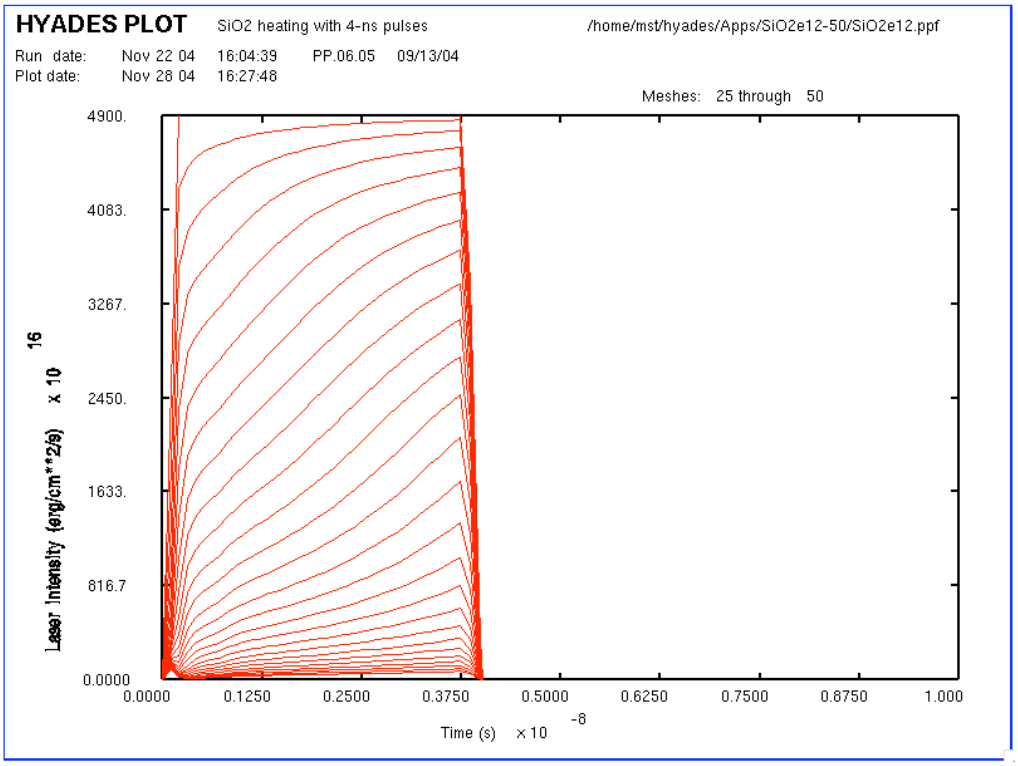

Figure 4. Time history of laser flux in the outermost half of the target for the Hyades base case

$$\alpha = 10^{-16}\, T_e^{-3/2}\, Z\, \ln\Lambda\, (n_e^2/n_{cr})$$

All units are cgs except temperature, which is measured in eV.

In a laser absorption wave, laser energy deposited at the wave front raises the electron temperature, allowing light propagation behind the front. [6] This occurs because the absorption coefficient drops as the plasma heats up. Based on Figures 1–4, the front half of the target appears to have burned through by the end of the pulse. This portion of the target maintains a temperature gradient, probably related to the exponential decay of the incident laser energy. The rear side of the target maintains a more uniform temperature as a result of radiation exhange at wavelenghts where the target is optically thinner.

As seen in Figure 2, the electron density shoots up rather quickly during the ramp-up phase and remains relatively constant at ~$5x10^{20}/cm^3$ over a portion of the laser pulse. Figures 5 and 6 help us to explain this behavior. Figure 5 shows the average charge state history in each zone. The entire target achieves a He-like state (Z_{eff}=8 for an average target Z of 10) very quickly, during the ramp-up phase, and then remains in that state until the laser is removed. At that point, the plasma slowly recombines. Notice that a gradual increase in charge state occurs during the laser pulse in the outermost 10 zones, which are most strongly heated (120-180 eV).

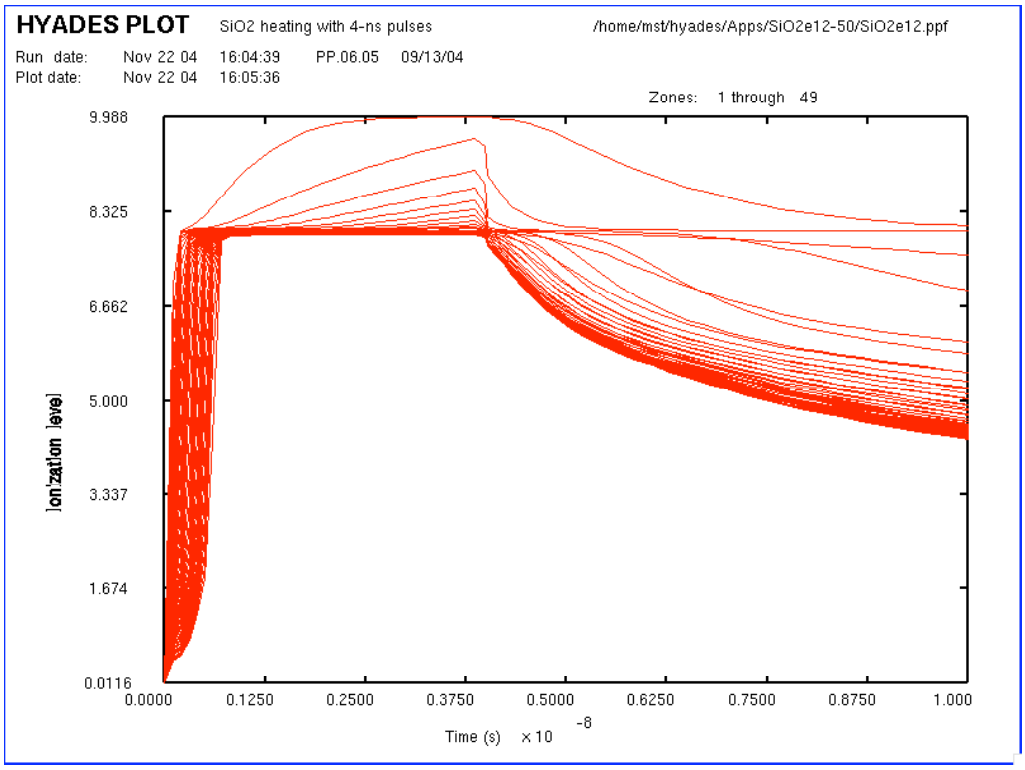

Figure 5. Charge state history at 50 equal-mass zones for the Hyades base case

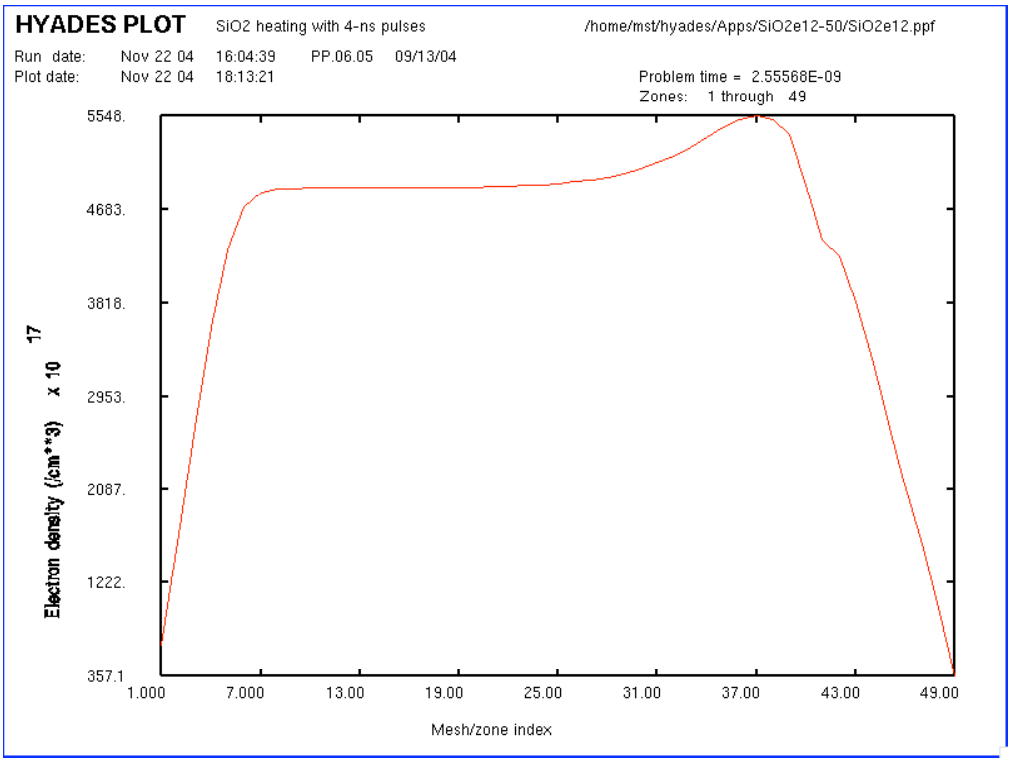

Figure 6. Electron density spatial profile at 2.5 ns for the Hyades base case

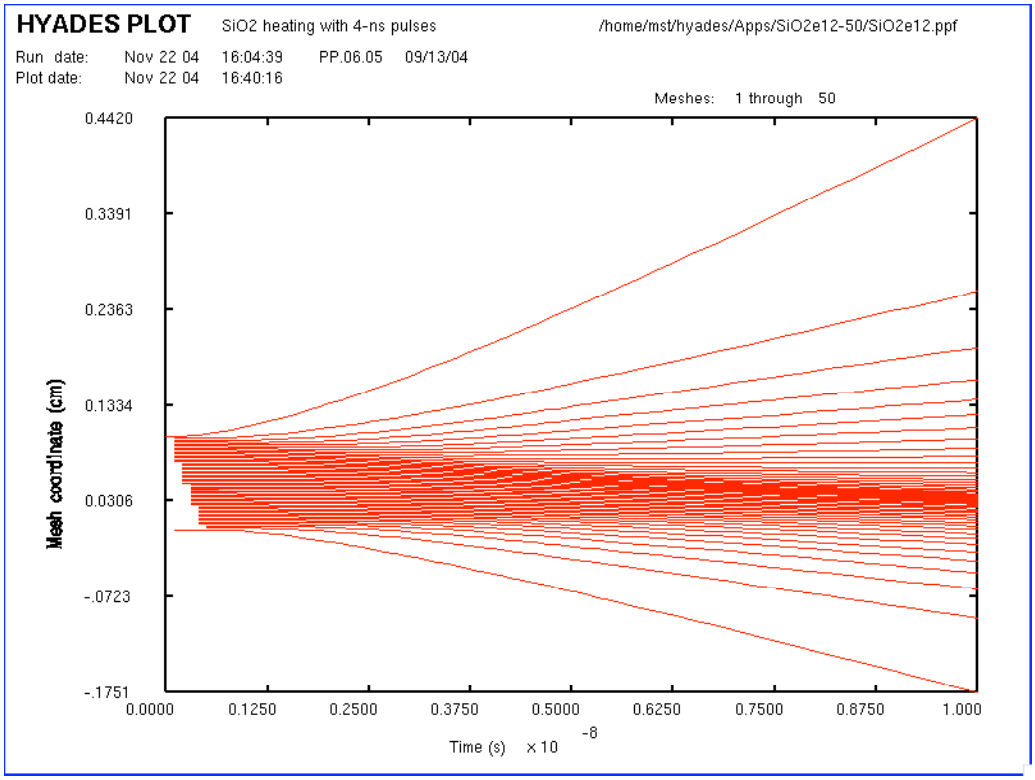

Figure 7. Time history of the radial location of the Lagrangian zones for the Hyades base case

Figure 6 helps to clarify the density history shown in Figure 2. It shows the spatial profile of electron density at 2.5 ns. The profile is relatively flat except at the outer edges. The curves in Figure 2 that drop down during the pulse are caused by hydrodynamic expansion on both sides of the target. For this value of laser intensity, the expansion velocity is relatively modest, such that the majority of the target remains intact even at the end of the 4-ns pulse. Figure 7 shows the R-t plot of the zones. It confirms that the outermost zones are expanding during the laser pulse, causing a rapid drop in density for those zones.

We examined the grid dependence of the Hyades results by running a case with 100 equally spaced nodes (instead of 50). The electron temperature and density histories are shown in Figures 8–9. The average charge state and R-t plots are nearly indistinguishable, and therefore are not shown here.

The temperature profile in Figure 8 is nearly identical to that of Figure 1, except for the outer-most zone in the 50-zone case. That zone appears to be considerably hotter than the case with a finer grid. The densities in Figure 9 are also very similar to those of Figure 2. The peak density is about 10% higher in the case with a coarse grid as compared with the finer grid. For the purposes of the parametric study shown in the following sections, we decided to use 50 zones because the results are easier to interpret without a separate graphical postprocessor (*i.e.,* using the existing HYADPLOT routine).

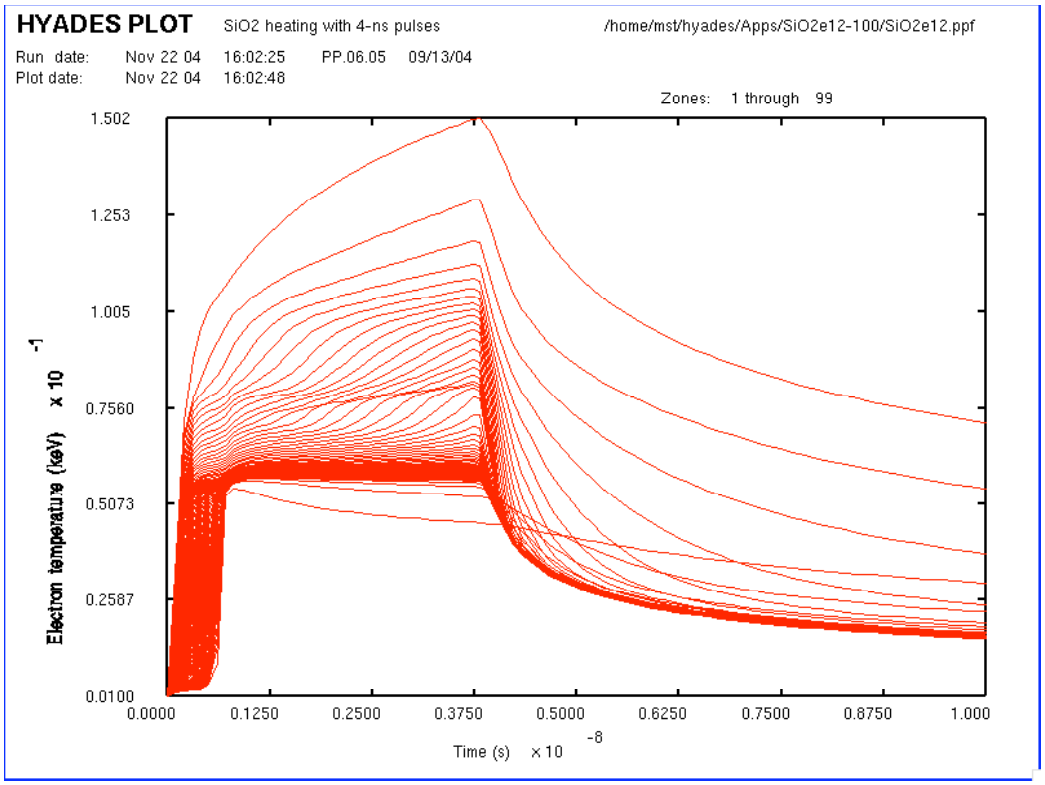

Figure 8. Electron temperature history at 100 equal-mass zones for the Hyades base case

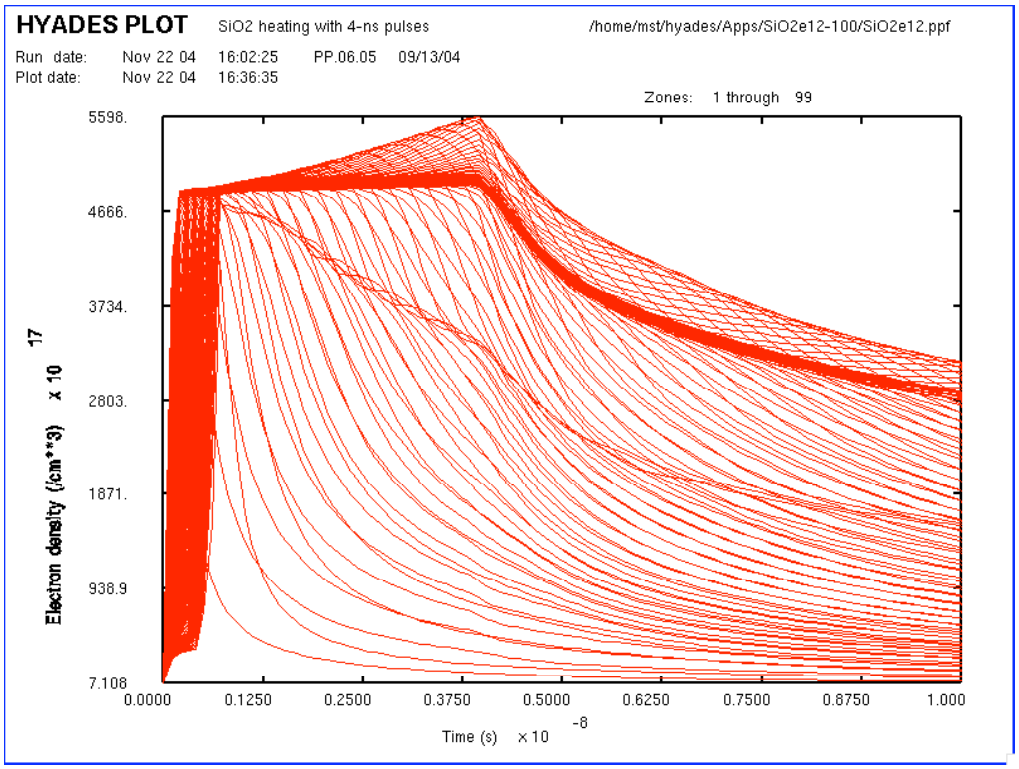

Figure 9. Electron density history at 100 equal-mass zones for the Hyades base case

2.1.2 Helios base case results

Helios provides a relatively independent check on the validity of the results presented in the preceding section. It includes laser absorption and hydrodynamic models similar to Hyades, but also provides spectrally resolved opacities as a built-in feature. We used the same input parameters for the Helios base case and a grid with 100 equally spaced nodes. Both the equation of state and spectrally resolved opacities were obtained from the PROPACEOS database. The default number of frequency groups was 50.

Figure 10 shows the electron temperature history corresponding to that of Figure 1. The peak temperature is ~215 eV as compared with 130 eV predicted by Hyades. Note that the temperature rises more slowly in the rear part of the target as compared with Hyades. Helios predicts continued heating of the rear side of the target in the late part of the laser pulse, whereas Hyades predicts a relatively flatter time history in the rear of the target. The temperature of the rear side increases nearly monotonically in time until it reaches almost 100 eV at the end of the pulse, whereas Hyades predicts a nearly constant 55 eV during the pulse. Most likely these differences arise due to the different opacity models used in Helios and Hyades.

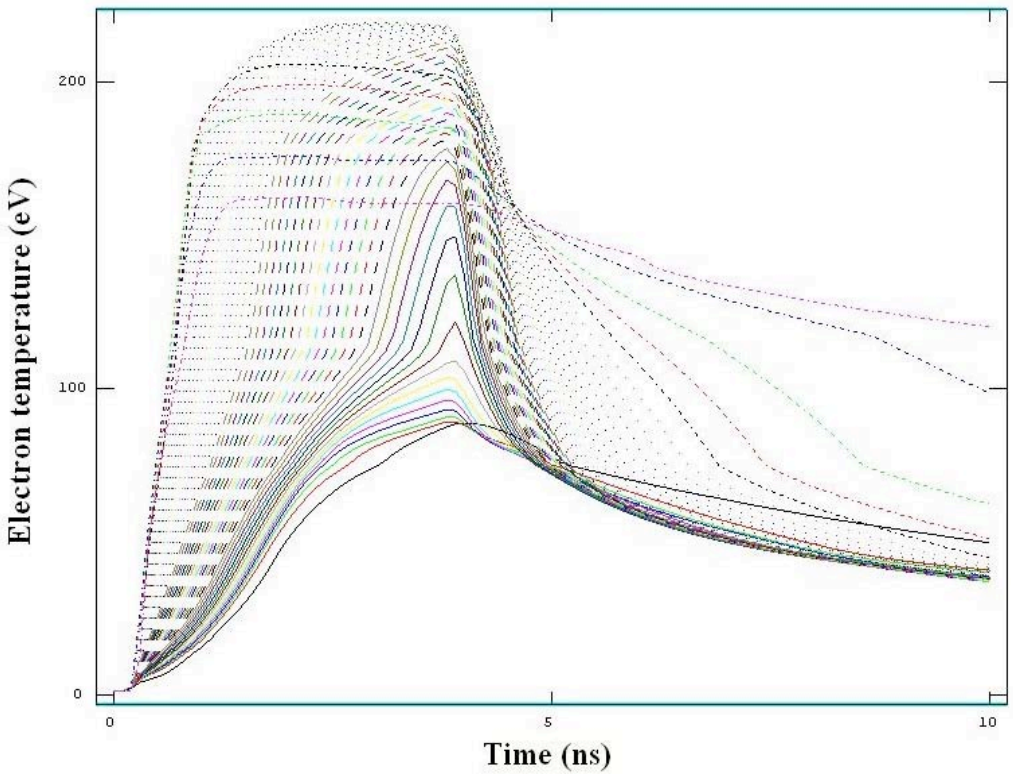

Figure 10. Electron temperature history for the Helios base case

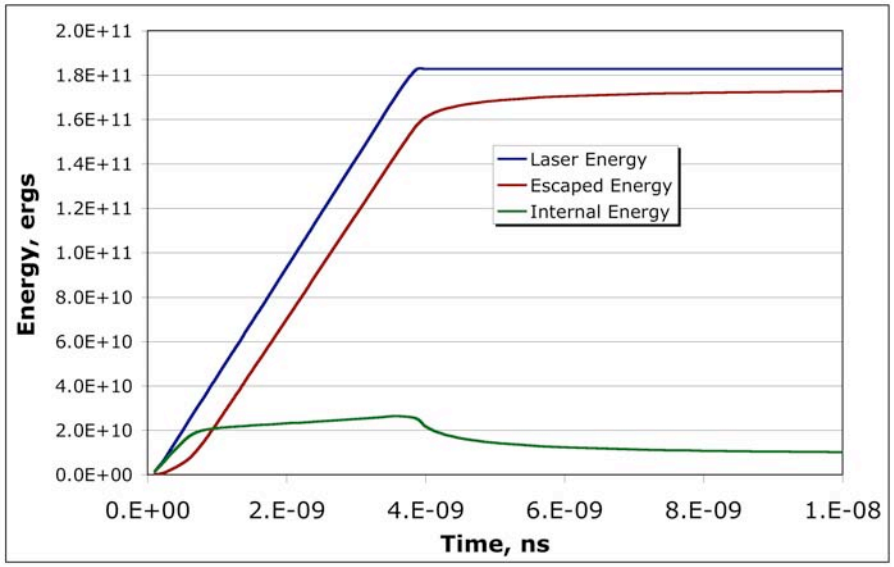

Figure 11. Internal and radiated energy for the Hyades base case

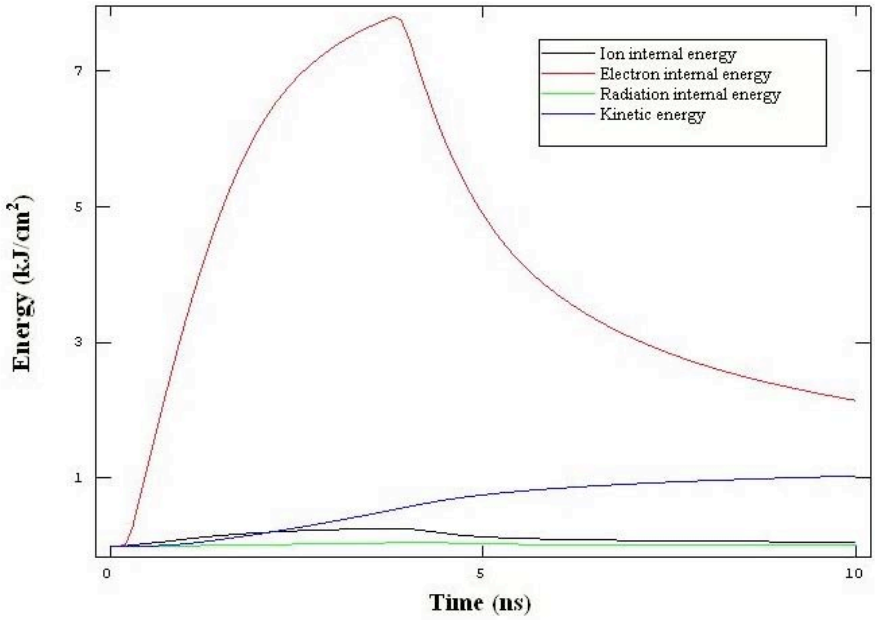

Figure 12. Internal energy for the Helios base case

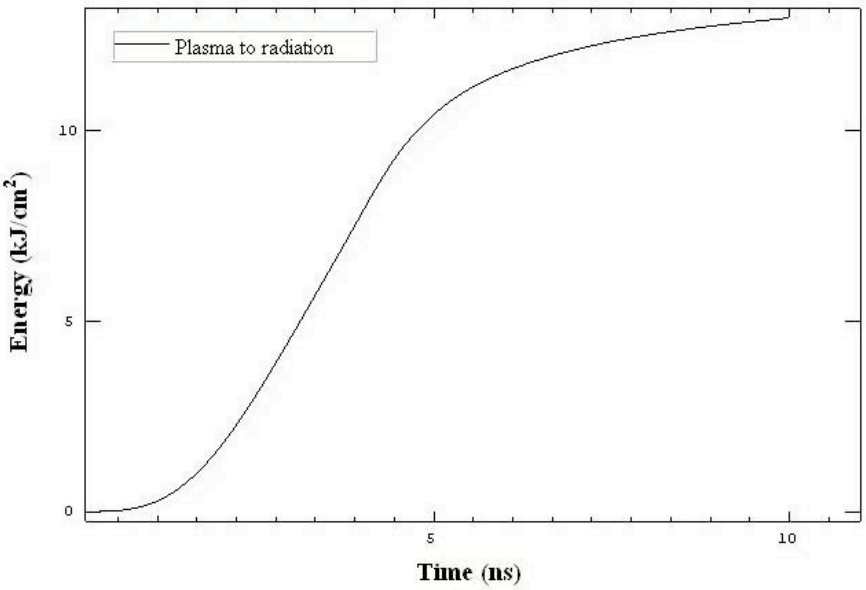

Figure 13. Radiated energy for the Helios base case

In order to elucidate the substantial difference in electron temperature between these two codes, we examined the energy balance *vs.* time for the modeling base case. Figures 11–13 show the evolution of internal energy and radiated energy for Hyades and Helios. The total energy for each is approximately equal to the incident laser energy of 18.6 kJ. Almost 90% of the incident laser energy promptly escapes by radiation in Hyades. After the initial heatup, the internal energy is modest, at about 10% of the total. Conversely, Helios predicts nearly *half* of the total energy during the laser pulse is retained in the electrons, with only half being promptly emitted.

As the plasma cools following the pulse, emission continues until a final state similar to Hyades is reached, with about 1 kJ (~5%) of energy in particle kinetic energy and the remainder radiated away.

Figure 14 shows the electron density history predicted by Helios, as compared with that of Figure 2. In this case, the agreement is remarkably good. The peak value of density ($5x10^{20}/cm^3$), as well as the temporal and spatial profiles, are very well matched. This is not entirely surprising, as the density is determined primarily by the charge state, which is relatively insensitive to temperature in this regime with a closed K-shell.

Helios consistently exhibits a rise in electron density within the target immediately after the laser source is removed. This appears to be caused by a recoil effect from the sudden change in pressure balance. Immediately after the laser is removed, hydrodynamic expansion near the two surfaces continues to push the target inward. This causes a mass density increase near the center, with a corresponding increase in electron density. This phenomenon is explored in more detail in Section 3.1 where the presence of dopant appears to enhance the effect.

Figures 15 and 16 are provided for comparison with the spatial profiles shown in Figures 3 and 5. Unlike Hyades, Helios predicts a drop in temperature at the front side closest to the plasma at 2.5 ns into the pulse. This cooling is plausible as a result of adiabatic expansion. As described above, the internal structure of the temperature profile is again evident: Hyades predicts a rather flat profile whereas Helios predicts a hotter (~200 eV) front side and colder (~100 eV) rear side.

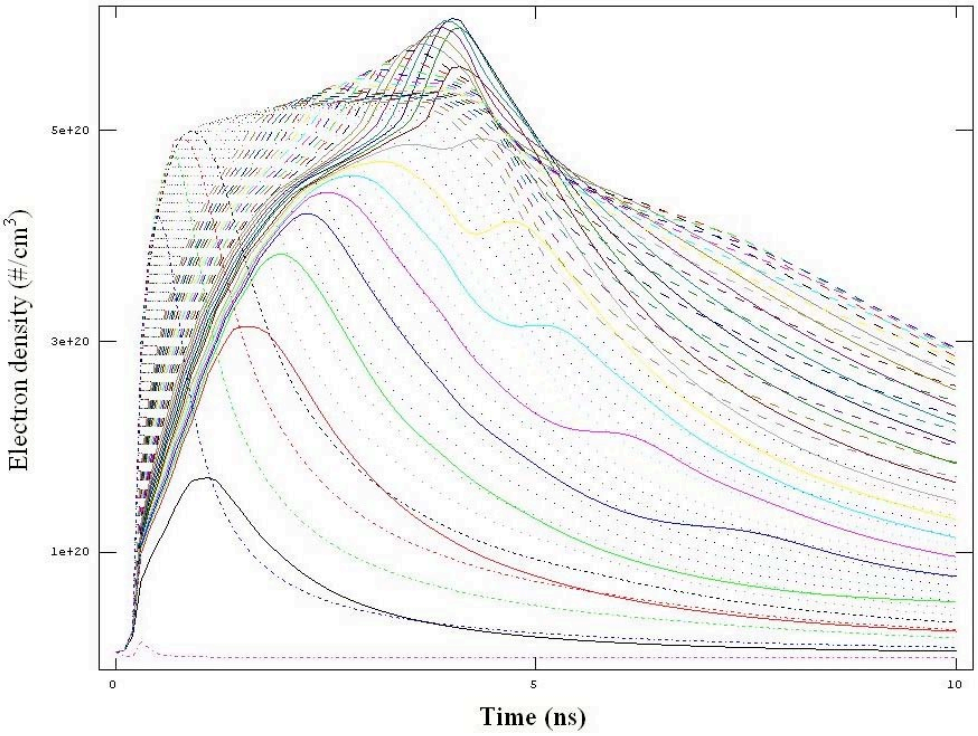

Figure 14. Electron density history for the Helios base case

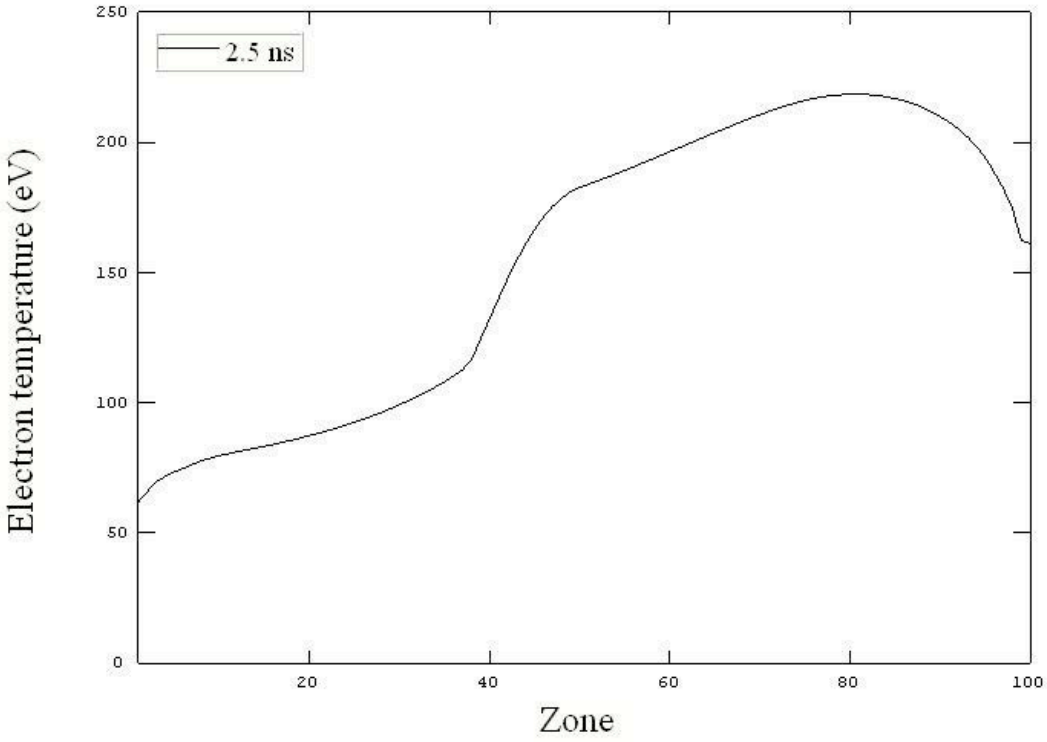

Figure 15. Electron temperature spatial profile at 2.5 ns for the Helios base case

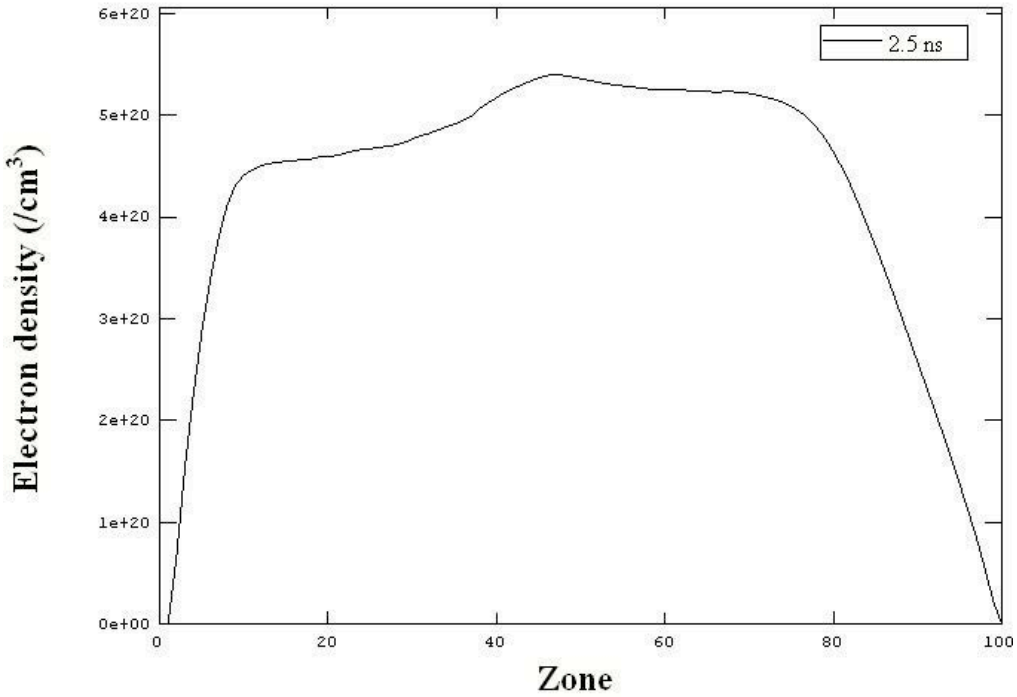

Figure 16. Electron density spatial profile at 2.5 ns for the Helios base case

2.2 Effect of opacity models on the base case results

Since radiation transport is one of the dominant mechanisms by which targets heat, cool and transport energy, treating the opacity, or absorption and re-radiation of photons is fundamental to determine the plasma evolution. In an effort to understand the differences between radiation transport driven by gray opacities *vs*. spectrally-resolved opacities, we attempted to swap input files between Hyades and Helios, and interpret the results. Not only would this allow us to assess the importance of full spectral resolution in modeling, but would provide a side-by-side comparison between two independent radiation hydrodynamics codes.

The following effects were explored:

1. We compared Hyades results using Rosseland average *vs.* Planck average opacities
2. We compared the Helios and Hyades models using identical Sesame data. This allows us to determine the extent to which differences are caused by the modeling approaches as opposed to the data used.
3. We attempted to model spectrally resolved results in Hyades using two different techniques: (a) group radiation transport with the built-in opacity model, and (b) imported data obtained from the Propaceos library. Neither of these approaches was successful.
4. We compared Helios results using spectrally resolved Propaceos data and single-group averaged data.

2.2.1 Opacity models and averaging techniques

There are two common methods for spectral averaging of opacities: Planck mean and Rosseland mean. The Planck mean opacity (a_p) is simply an average over wavelengths, which is weighted by a blackbody spectrum ($e_{\lambda b}$) [7]:

$$a_p(T,n) = \frac{\int_0^\infty a_\lambda(\lambda,T,n)\, e_{\lambda b}(\lambda,T)\, d\lambda}{\sigma T^4}$$

where the spectrum is given by:

$$e_{\lambda b} = \frac{2\pi C_1}{\lambda^5 (e^{C_2/\lambda T} - 1)}$$

It is most useful for estimating emission, and in some optically thin cases. The Rosseland mean opacity (a_R) is a flux-weighted average of the diffusivity (inverse of absorption):

$$\frac{1}{a_R(T,n)} = \frac{\int_0^\infty \frac{1}{a_\lambda(\lambda,T,n)} \frac{de_{\lambda b}}{dT}(\lambda,T)\, d\lambda}{\int_0^\infty \frac{de_{\lambda b}}{dT}(\lambda,T)\, d\lambda}$$

where the derivative of the Planck spectrum can be written as:

$$\frac{de_{\lambda b}}{dT} = \frac{2\pi C_1 C_2}{\lambda^6 T^2} \frac{e^{C_2/\lambda T}}{(e^{C_2/\lambda T} - 1)^2}$$

Rosseland mean opacity is more appropriate in cases which are dominated by radiation diffusion (which is the form of radiation transport assumed in Hyades as the default). Figure 17 shows the two averaged opacities as a function of temperature for a density of 2 mg/cm^3 in SiO_2 using Sesame data. The Planck mean is higher at lower temperatures, but drops off quickly above about 1 keV. The Rosseland mean opacity remains finite at very high temperatures.

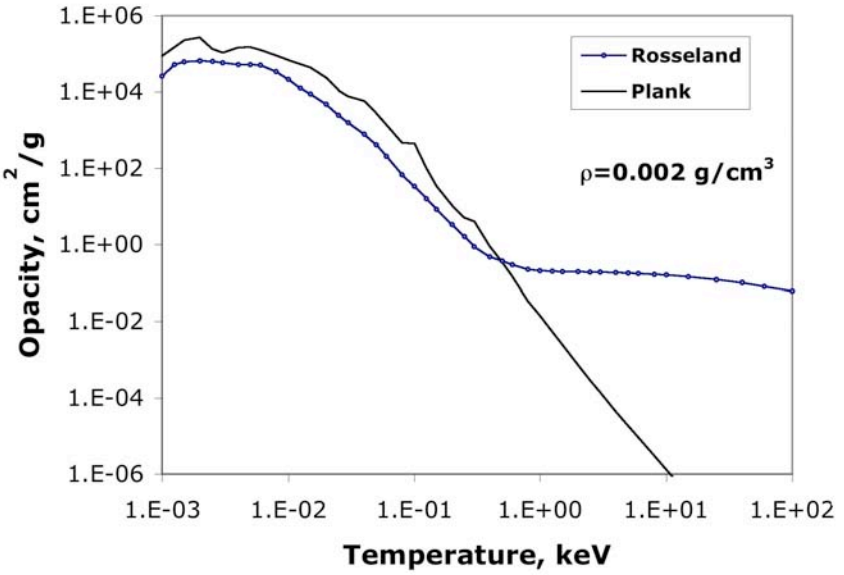

Figure 17. Comparison of Rosseland and Planck Sesame opacity for SiO_2

Helios allows the user to implement spectral averaging in the code by choosing a single frequency group in the input parameters. The type of averaging is determined automatically by the code; the user has no control over this. In order to examine the single-group Planck and Rosseland averages, we wrote a short Fortran routine to perform the averages from the full Propaceos data files. Appendix B.2 contains the source code listing. Figures 18 and 19 compare the Sesame single-group opacities with the averaged opacities we calculated from Propaceos. The Propaceos data is consistently higher than Sesame in the range of 100–1000 eV, which is an important range of energies for the present work. This could easily explain the substantial differences observed in the electron temperature and energy balance.

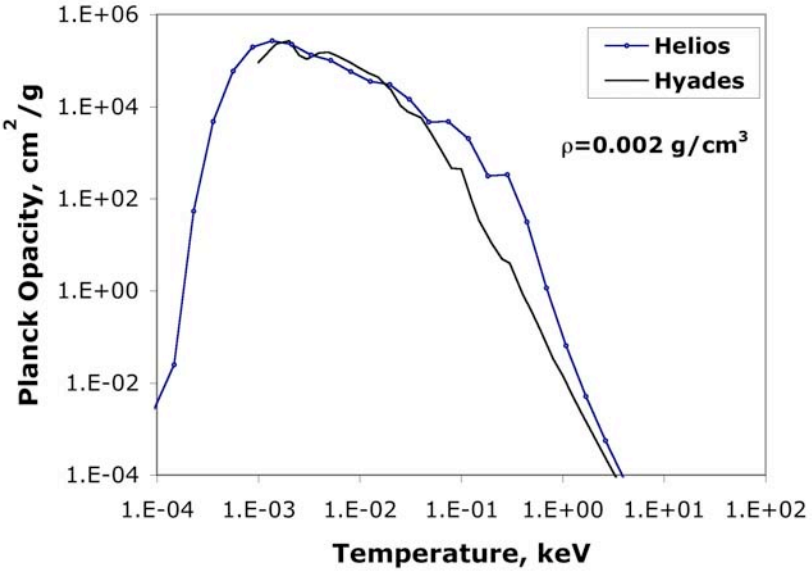

Figure 18. Comparison of single-group Sesame and Propaceos data with Planck averaging

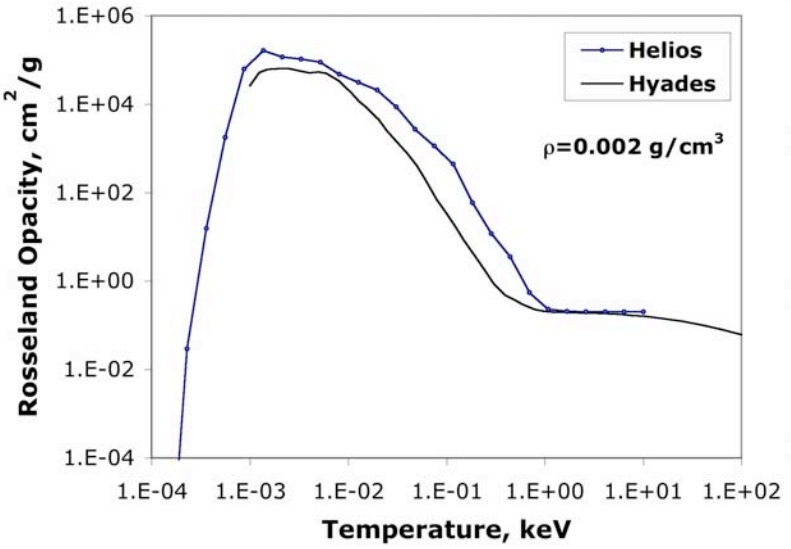

Figure 19. Comparison of single-group Sesame and Propaceos data with Rosseland averaging

2.2.2 Comparison of Hyades results with Planck vs. *Rosseland averaging*

Rosseland mean averaged data are the default used by Hyades. However, the optical thickness of some of our plasmas is rather small, and so Planck averaged data may be more appropriate. We ran the base case with Planck averaged Sesame data for comparison. Figure 20 shows the electron temperature profile through the target at 2.5 ns into the pulse. Comparing with Figure 3, the results are very similar. Differences are at the level of 10%.

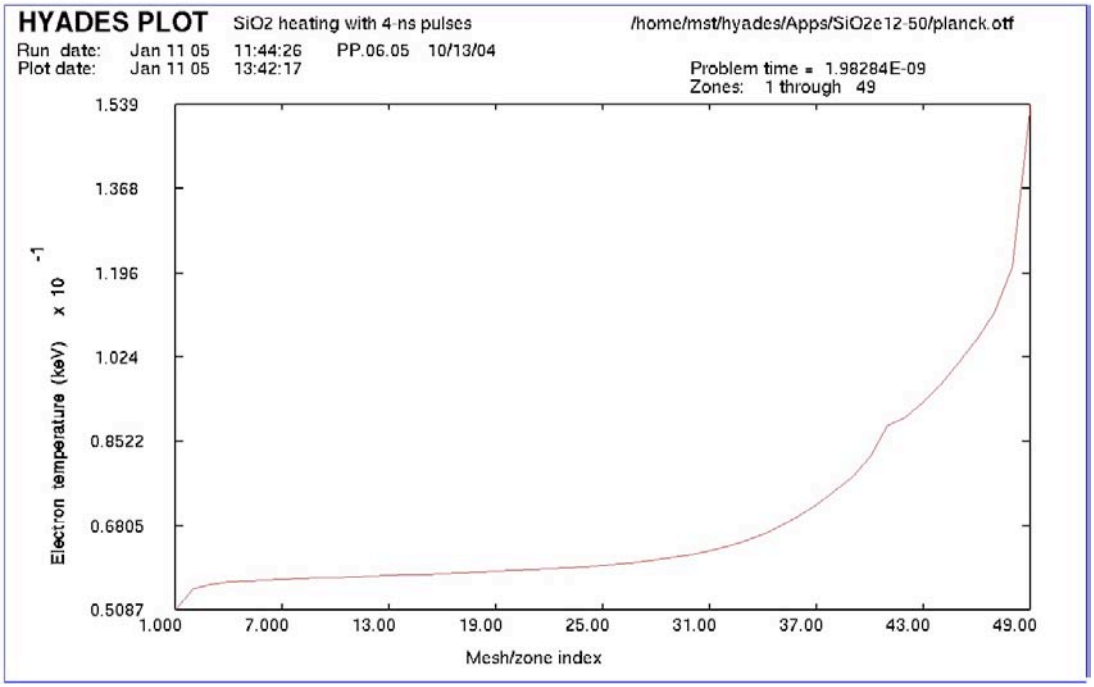

Figure 20. Hyades electron temperature at 2.5 ns using single-group Planck averaging

2.2.3 Comparison of Hyades and Helios models using identical (gray) Sesame data

Importing gray opacities from the Hyades Sesame library into Helios allows us to directly compare the results from two laser-plasma simulation codes using identical input data sets (Sesame EOS and opacity). It also provides some insight into whether or not single-group opacity tables are sufficient in capturing the radiation signature of under-dense plasmas.

We wrote a simple C++ program that extracted single-group opacity data from the Hyades Sesame library and reformatted it for Helios. Below are the results from Helios using Sesame EOS and opacity data. For comparison, results from the analogous Hyades run (identical input data) are shown in Figures 1–4.

As shown in Figures 21 and 22, the densities for these runs are approximately the same. A more surprising result is that the peak electron temperature for the Helios run is more than a factor of 3 higher than that of the Hyades run (see Figures 23 and 24). Since the input data sets are identical, this difference can only be attributed to the internal algorithms of the codes; *i.e.,* laser energy absorption processes, ionization models, energy coupling between radiation field and electrons, *etc*. *We are continuing to explore this surprising result.*

Comparing Figures 21–24 with Figures 1–3 and 6, we can establish the difference in target behavior with the same code but different opacity datasets. Using Sesame data, temperatures predicted by Helios are over a factor of two higher. Electron densities are more similar, with changes of the order of 10%. As we observed earlier, the electron density is relatively insensitive to temperature when the atoms are stripped down to a closed shell.

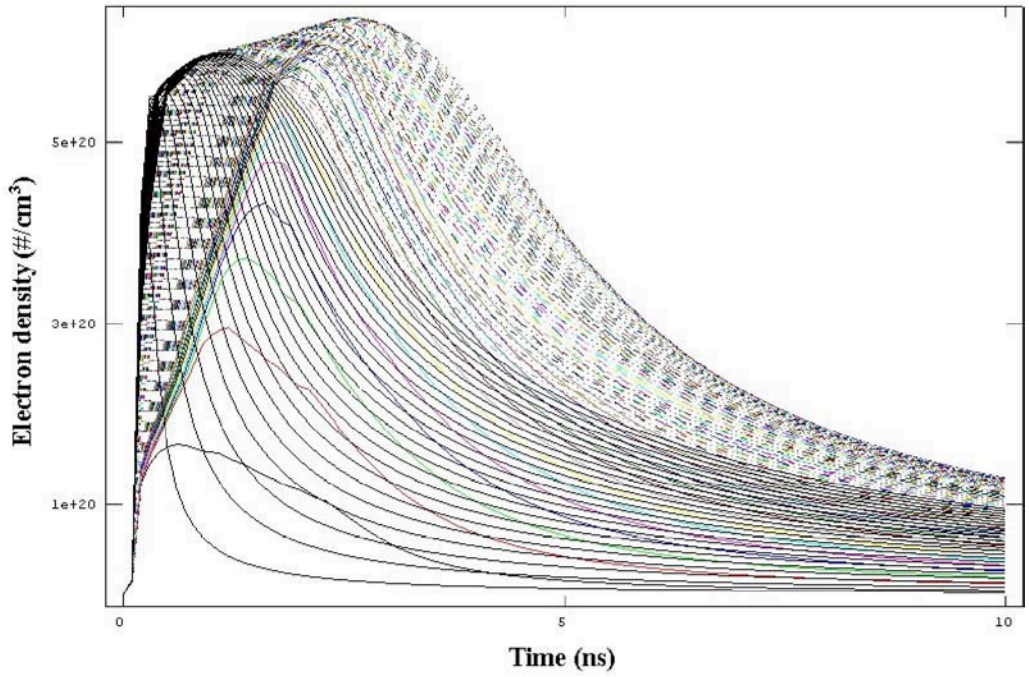

Figure 21. Electron density history for Helios using Sesame gray opacity and EOS

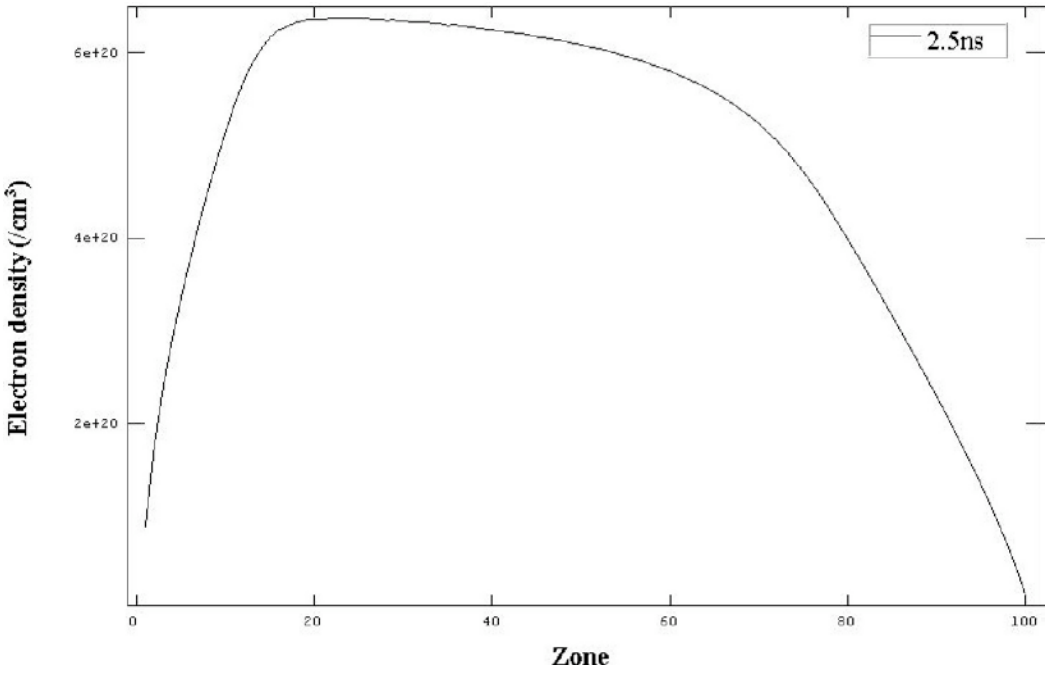

Figure 22. Electron density spatial profile at 2.5 ns for Helios using Sesame gray opacity and EOS

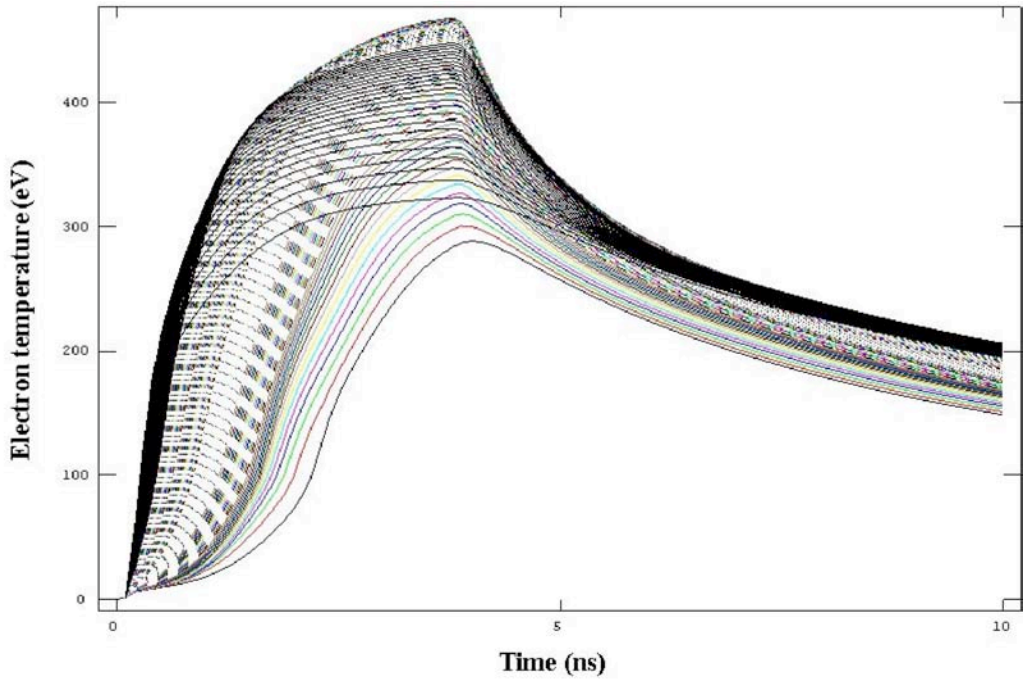

Figure 23. Electron temperature history for Helios using Sesame gray opacity and EOS

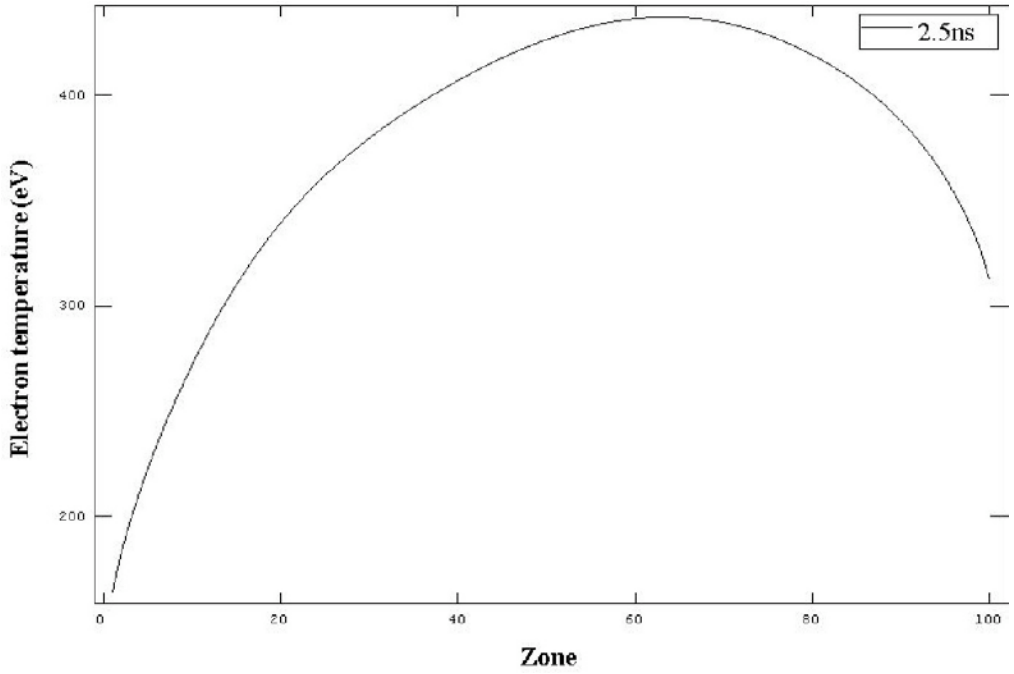

Figure 24. Electron temperature spatial profile at 2.5 ns for Helios using Sesame gray opacity and EOS

2.2.4 Attempts at spectrally resolved results with Hyades

A typical Hyades run uses spectrally averaged EOS and opacity data extracted from the Sesame data library. User options are offered for multi-group radiation transport and spectrally resolved opacities. Attempts were made to introduce spectral resolution into Hyades *via* these two techniques. First, group radiation transport was attempted using the built-in multi-group transport model, and second, attempts were made to import spectrally resolved data from the Propaceos library.

When a GROUP statement is included in the HYADES input file, opacity data is generated using an internal algorithm which includes some atomic shell effects and crude x-ray line effects. We specified 100 spectral groups with a maximum energy of 3 keV, using the following input statement:

```
group 1 100 9.8e-5 3.0
```

All other input parameters remained identical to the base case. Figure 25 shows the electron temperature history resulting from this run. The maximum temperature rose to over 500 eV in this case. The most likely cause of such an unexpectedly high electron temperature is the presence of lower radiation emission. Radiation emission is the primary energy loss term which balances energy absorption by inverse bremsstrahlung; with reduced emissivity, the temperature will rise until the radiation emission equals the laser input power.

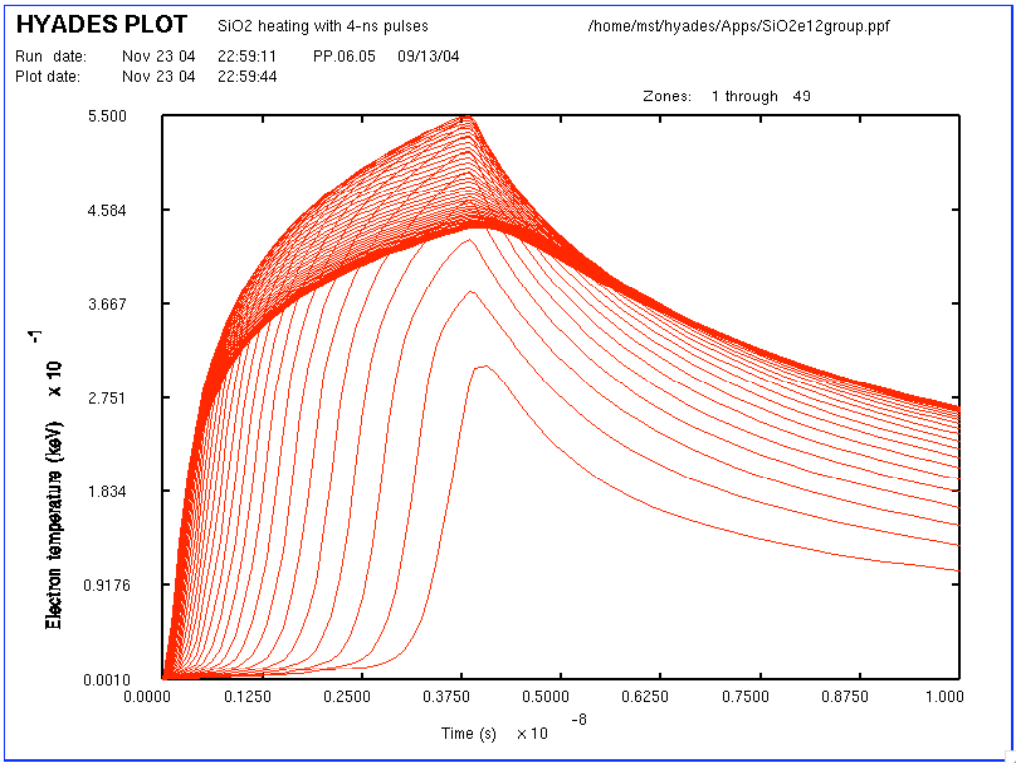

Figure 25. Electron temperature history using the Hyades group radiation transport module

The peak temperature achieved with Hyades using group radiation transport is similar to the temperature found with Helios using gray opacities. Most likely this is a coincidence coming from two separate effects.

Figure 26 shows the corresponding charge state of the plasma. The higher temperature causes the SiO_2 to rapidly strip to a fully ionized state. There is little delay at the He-like charge state of 8. The electron density in this case is a strongly varying function of both time and space.

In a second attempt to implement a spectrally resolved treatment of radiation, we tried to import data from PROPACEOS into Hyades. Hyades explicitly supports the option of importing an external spectrally resolved file in ASCII format. For simplicity, a routine was created with IDL (Interactive Data Language) to perform the conversion of the Propaceos file into a Hyades-compatible format. The content of the converted file was re-read and plotted with IDL, and was determined to match Helios data-viewer plots of the original Propaceos file.

A record was added in the HYADES input file to call the external opacity file directly by specifying its path and filename in the "EOS" record. We were not able to obtain results using this technique. Although the code supports externally generated multi-group opacity tables in principle, the import utility failed in mapping the data into a run. We are attempting to resolve this problem with the author of the code. In addition, the option of mapping the ASCII data into the binary opacity library is being explored.

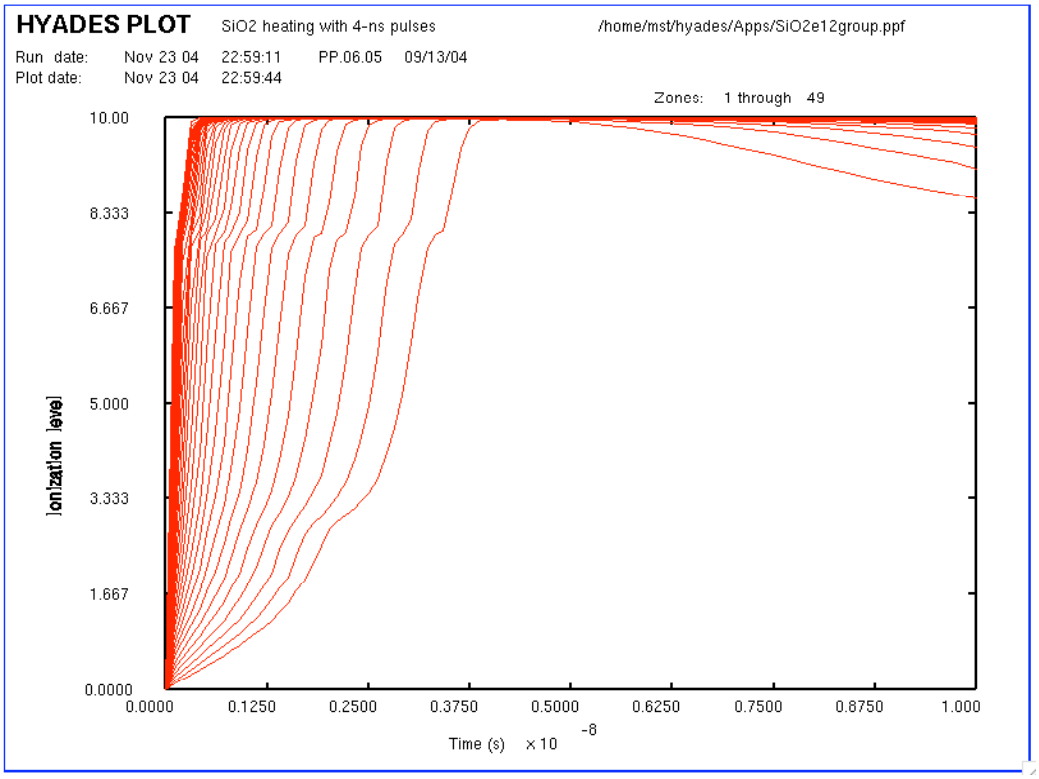

Figure 26. Charge state history using the Hyades group radiation transport module

2.2.5 Comparison of gray vs. spectrally-resolved opacities in Helios

The standard model in Helios uses spectrally resolved data from the PROPACEOS code. In Section 2.2.3, we showed results from Helios using Sesame gray opacities and compared those results with the spectrally resolved run. This helped to elucidate differences between Hyades and Helios, but is not a good test of the effect of spectral detail. Sesame and PROPACEOS data sets are obtained from different sources, and are therefore inherently different.

In this section we compare Helios results using three different levels of spectral detail. In Section 2.1.2 we already displayed results from the base case, in which 50 frequency groups were used. Here we add a case with 500 frequency groups and a case with one frquency group. The latter case is equivalent to using a Rosseland mean (gray) opacity.

The electron temperature history for the single-group case is shown in Figure 27. The temperature is about 5% lower that the base case, but otherwise very similar. Electron temperature is the most important parameter, and the one we have observed to depend the most on the data and models. Therefore, we conclude that the effect of spectral averaging is very minor. Inspection of the other parameters showed few discernable differences.

The electron temperature profile for the 500-group case at 2.5 ns is shown in Figure 28 together with the same profile for the single-group case. Except for the presence of a bump in temperature near the target center, the results are quite similar. The spectrally resolved case exhibits about 5% higher temperature in general.

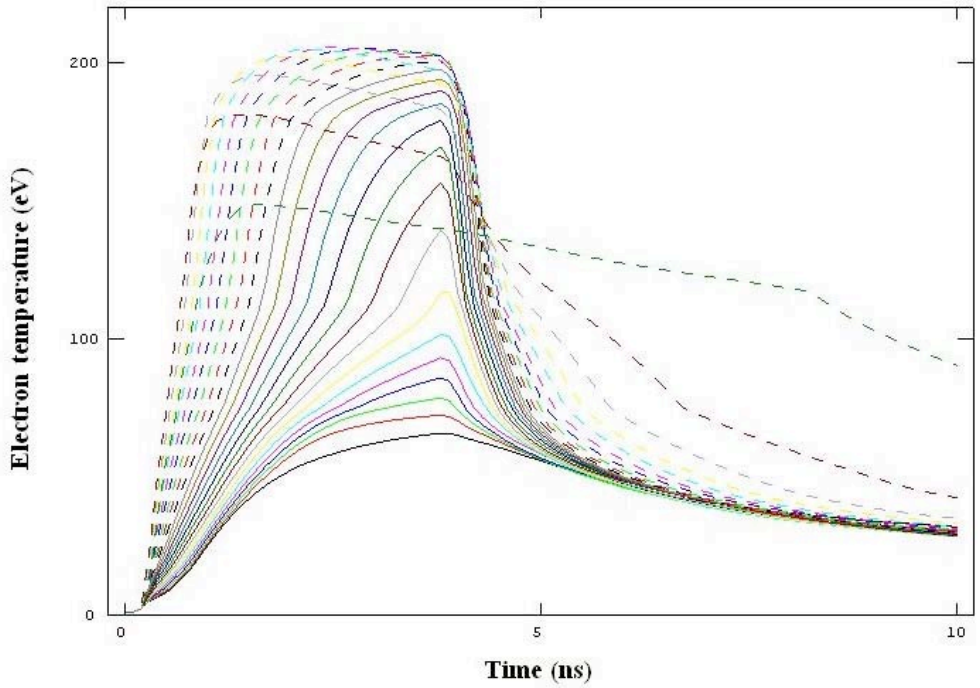

Figure 27. Electron temperature history from Helios using a single radiation group

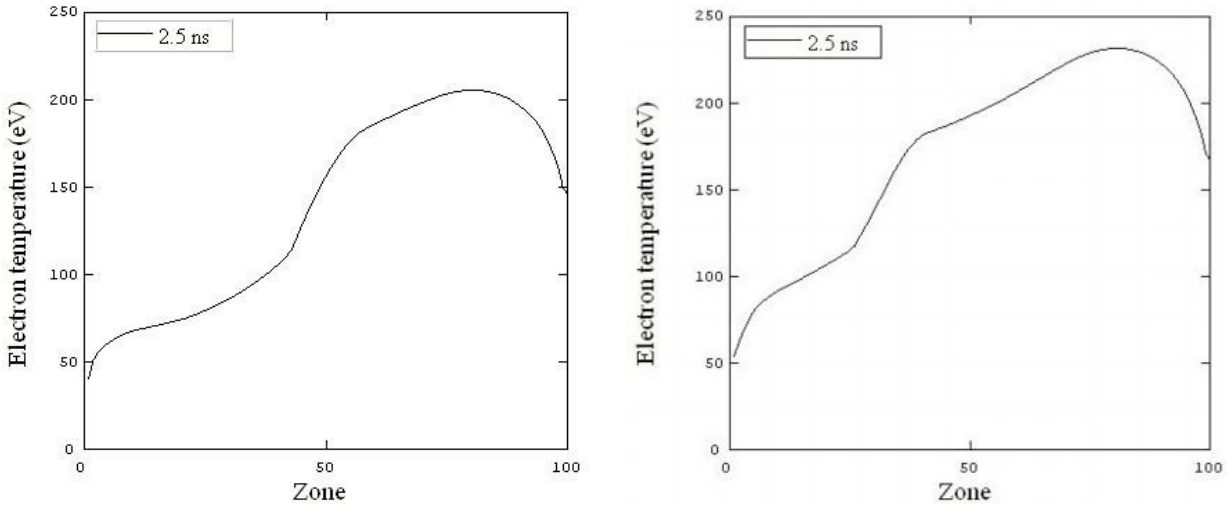

one group *500 groups*

Figure 28. Comparison of electron temperature profiles using one or 500 radiation groups

3. Variation of parameters

3.1 Addition of dopant

3.1.1 Gray opacity results with Hyades

The experimental conditions of interest include doping of either 2% or 6% Ti by weight in a SiO_2 carrier. As discussed in Section 2.2.4, we were not able to input spectrally resolved opacities in Hyades, and results using the built-in multi-group transport algorithm were questionable. Therefore, Hyades modeling of the effect of a dopant was restricted to spectrally averaged cases. In order to model a mixture of Ti and SiO_2 in Hyades, we needed to generate new EOS and opacity data tables, as they are not included with the Hyades distribution. We used an arithmetic, density-weighted average to generate new EOS and gray opacity tables. Appendix B.3 contains a listing of the Fortran code we used to perform this averaging.

Figures 29–30 show the Rosseland mean opacity (the default opacity model used in Hyades) and internal energy as a function of temperature at a density of 0.002 g/cm^3. Although the opacity of Ti is somewhat different than SiO_2 at lower temperatures, the averaging leads to nearly indistinguishable behavior for SiO_2-6% Ti as compared with pure SiO_2. The pressure and energy are even less affected. Based on the similarity of the data, we would not expect different radiation hydrodynamic behavior using gray opacities in Hyades.

Nevertheless, we ran a case with 6% Ti in order to demonstrate the differences quantitatively. Indeed, there is little difference. Figures 31 and 32, which show n_e and T_e at 2.5 ns, are representative of the differences. The use of gray opacities apparently leads to changes in plasma conditions roughly in line with the fraction of dopant – only a few percent.

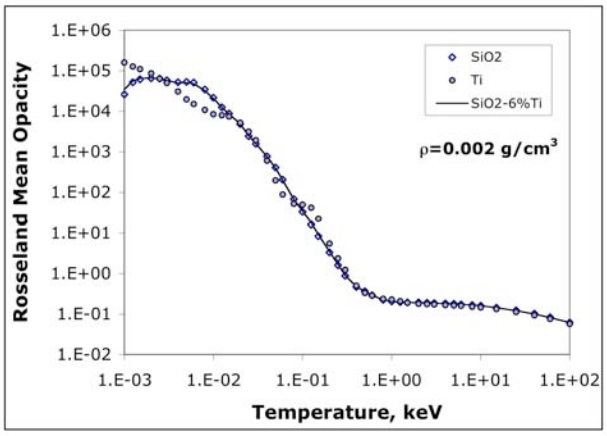

Figure 29. Rosseland mean opacity for SiO_2, Ti and a mixture of SiO_2-6%Ti

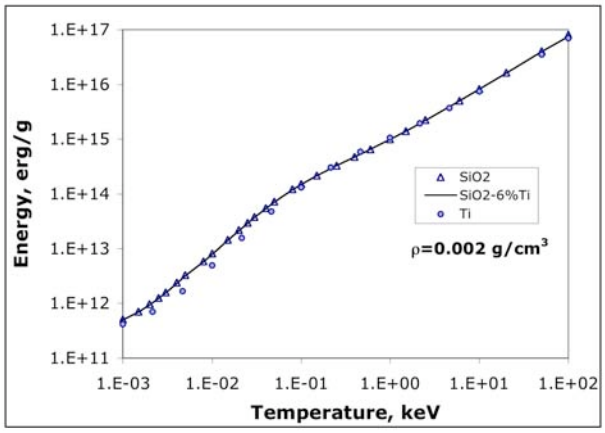

Figure 30. Internal energy EOS for SiO_2, Ti and a mixture of SiO_2-6%Ti

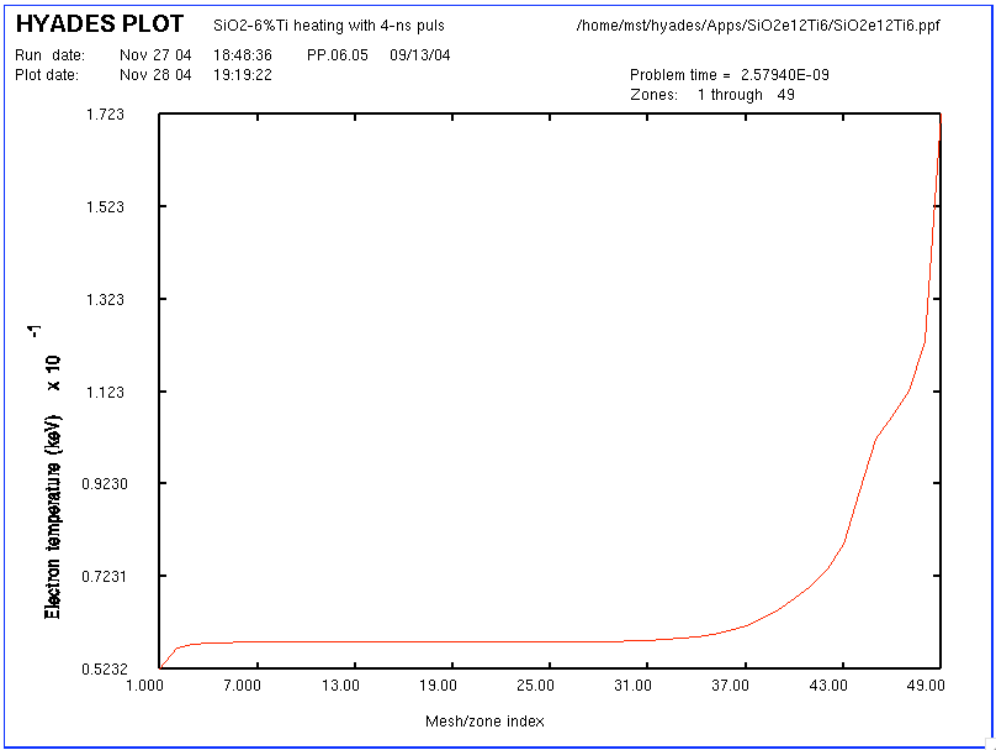

Figure 31. Electron temperature profile at 2.5 ns for SiO_2-6%Ti using gray opacities in Hyades

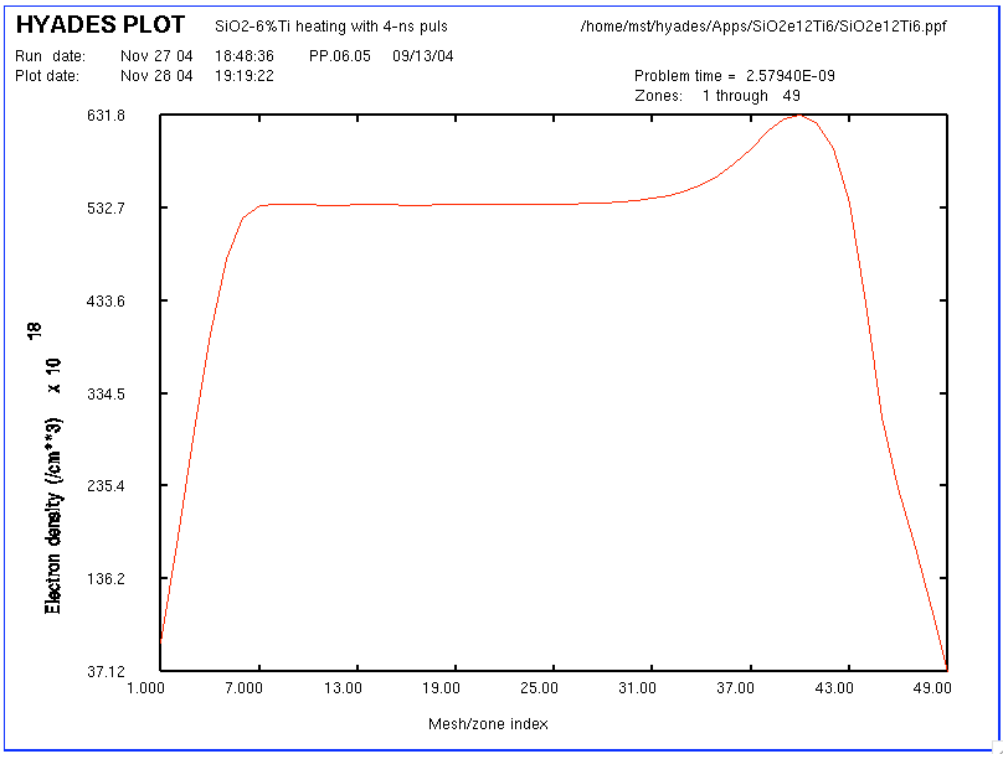

Figure 32. Electron density profile at 2.5 ns for SiO_2-6%Ti using gray opacities in Hyades

3.1.2 Spectrally resolved results with Helios

Helios includes spectrally resolved opacities from the PROPACEOS code. We obtained EOS and opacity data for mixtures of 2 w/% and 6 w/% Ti from Prism Computational Sciences and used these to compare with the base case.

Comparing Figure 33-34 with Figures 10 and 14, we can see a general decrease of electron temperature of about 25% for the case with 6% Ti doping. The case with 2% doping, shown in Figure 35, exhibited about 10% reduction in temperature. The temperature drop is most noticeable in the central region of the target. At present we do not have an explanation for this phenomenon.

The density profile, shown in Figure 36, exhibits some minor changes as compared with the base case. The magnitude remains in the range of 4–5 x $10^{20}/cm^3$, with clear evidence of hydro expansion at 2.5 ns into the pulse. The peak occurs nearer the laser in the case of doping, which tends to indicate a change in the pressure balance.

Overall, the hydrodynamic behavior is changed only modestly by the inclusion of Ti doping up to 6%. The magnitude of temperature drops slightly, and the profile becomes more nonuniform. Changes in density indicate internal hydrodynamic motion has changed; these changes are of the order of 10-20%.

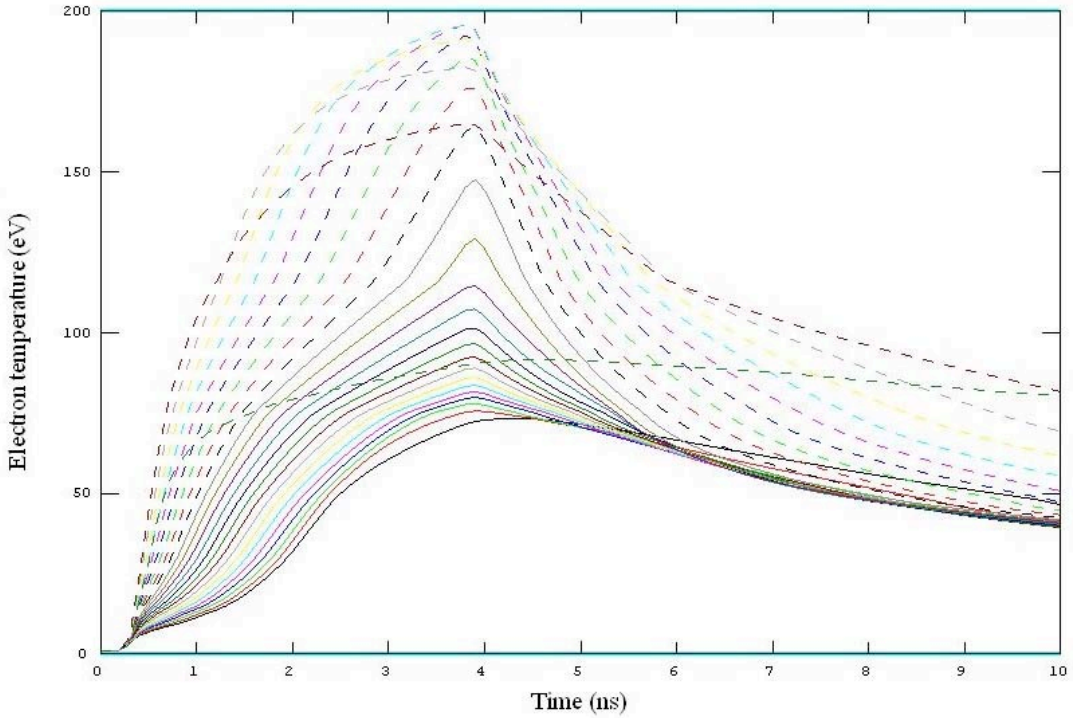

Figure 33. Electron temperature history for SiO2-6% Ti using Helios

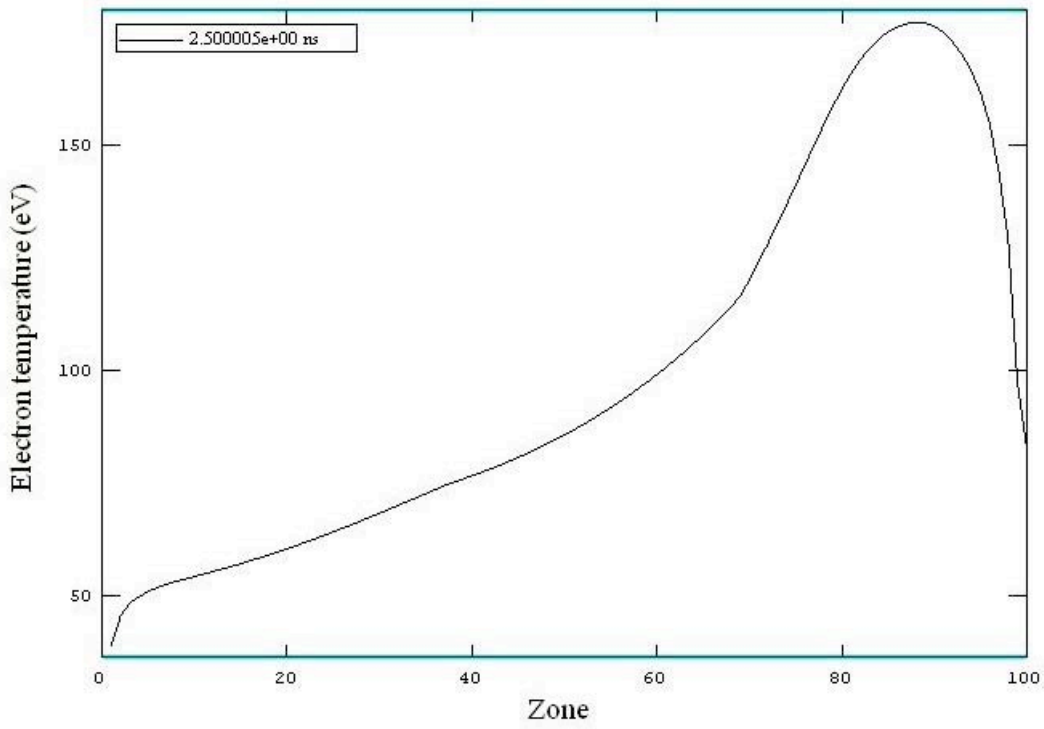

Figure 34. Electron temperature spatial profile at 2.5 ns for SiO2-6% Ti using Helios

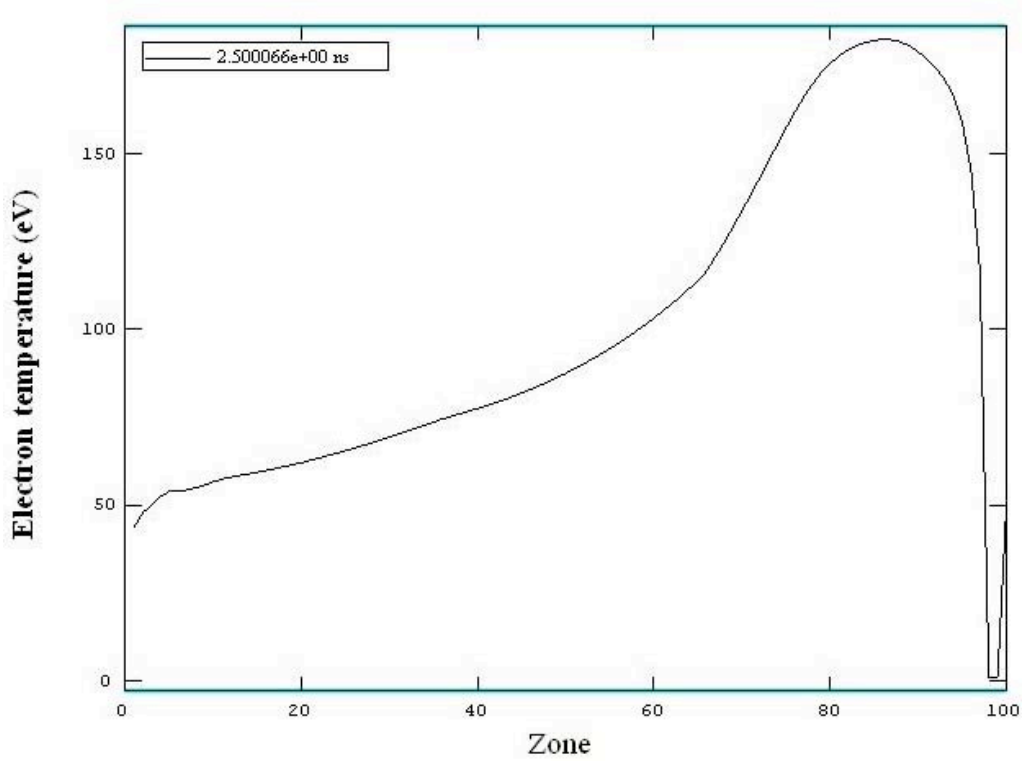

Figure 35. Electron temperature spatial profile at 2.5 ns for SiO2-2% Ti using Helios

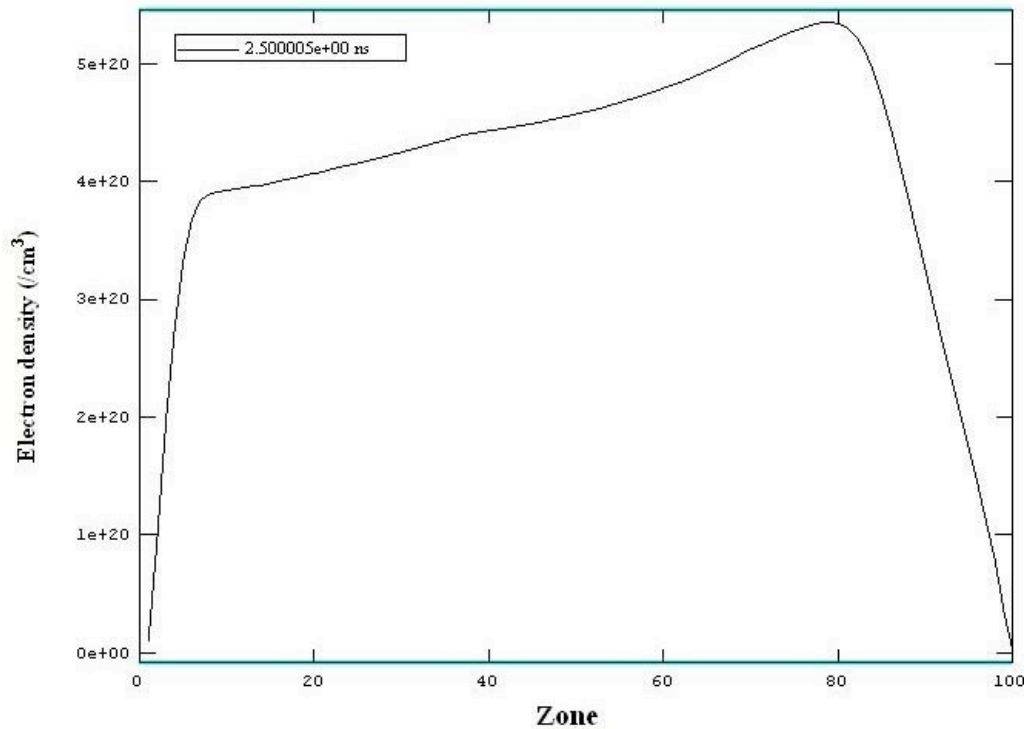

Figure 36. Electron density spatial profile at 2.5 ns for SiO2-6% Ti using Helios

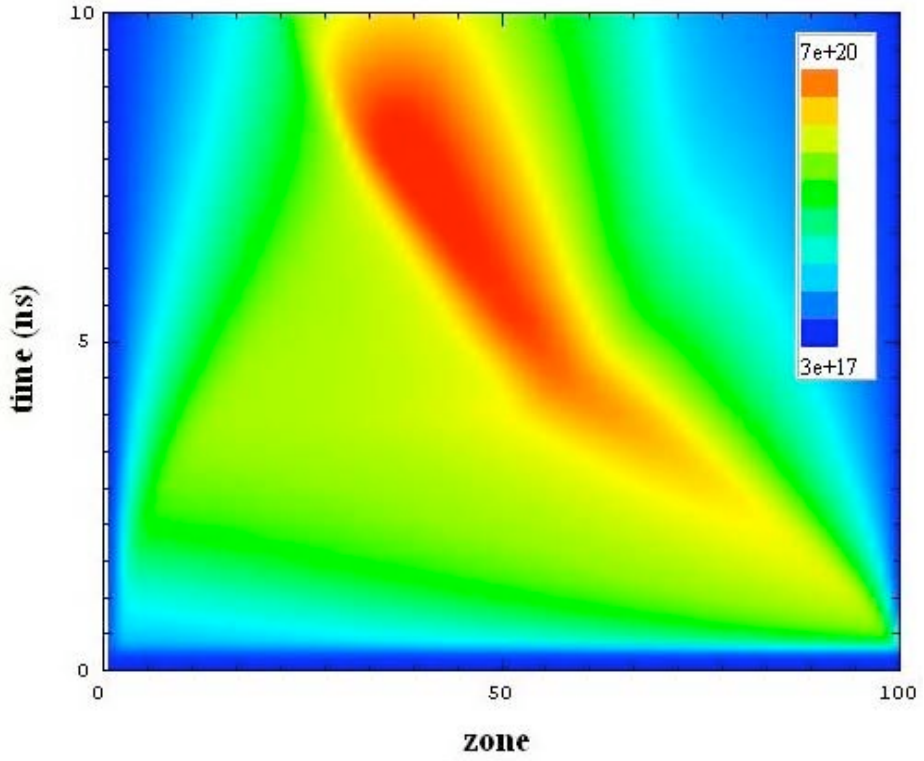

Figure 37. Contour plot of electron density for the 6% Ti case

As discussed in Section 2.1.2, we noticed a tendency for the electron density to rise in the central part of the target *after the laser is removed*. Figure 37 shows a color contour plot of the time and space dependence of electron density. The increase in electron density tracks an increase in mass density, which indicates that the target is being compressed toward the center by hydrodynamic blowoff on each end.

3.2 Increase in SiO_2 density from 2 to 8 mg/cm^3

The second experimental parameter we varied was the density of the target. As shown in Figure 4, the laser is not penetrating into the target very well even for the case of 2 mg/cm^3. Not surprisingly, Figure 38 shows even strong absorption at 8 mg/cm^3. Only the outermost 5 nodes directly absorb the laser. Figure 39 shows the evolution of electron density.

After 2.5 ns, the target electron density is remarkably flat, with a value approximately four times higher than the 2 mg/cm^3 targets. The charge state, similar to that of Figure 5, remains He-like during the majority of the pulse. The electron temperature profiles are also quite uniform after about 2.5 ns. The temperature of the front side of the target is depressed as compared with the 2 mg/cm^3 case, but still quite uniform. Figure 39 shows a similar behavior for the electron density.

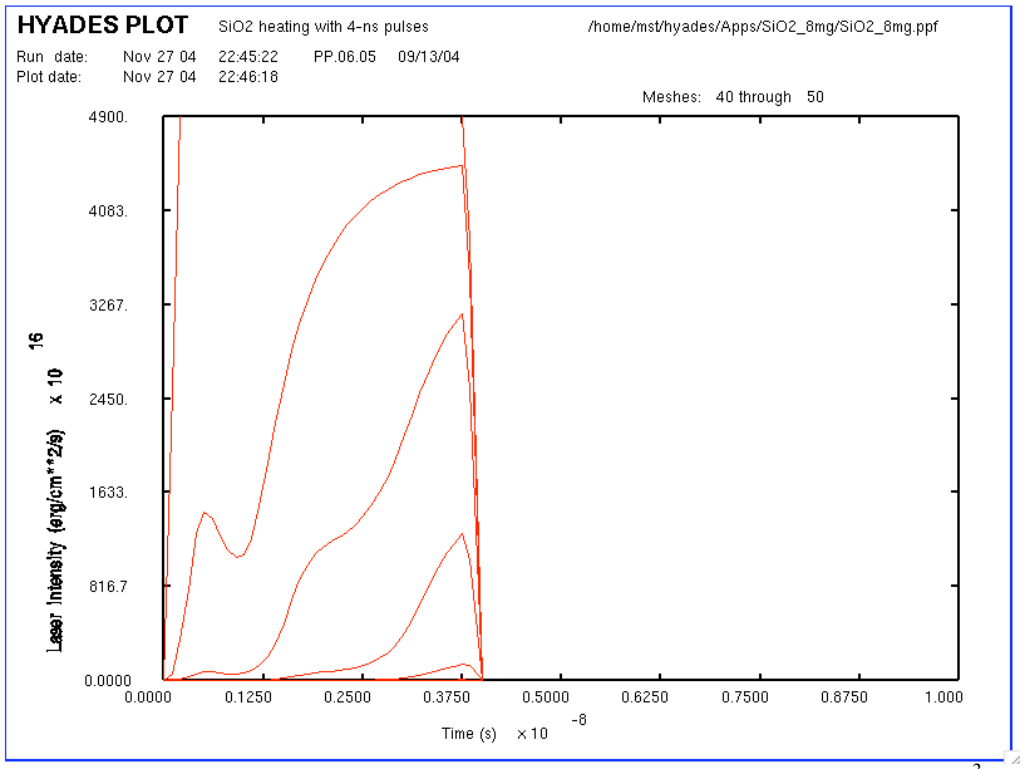

Figure 38. Time history of laser flux in the outermost 10 nodes of the 8 mg/cm^3 target

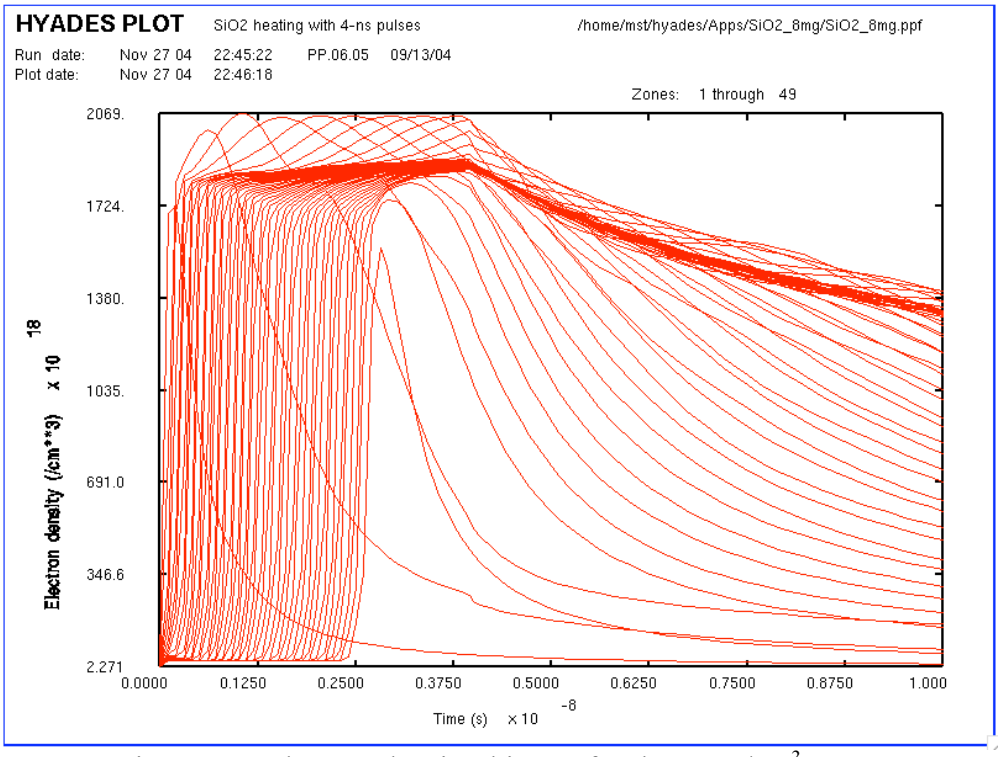

Figure 39. Electron density history for the 8 mg/cm^3 target

Figure 40 clearly shows the process of burn-through. Target heating in this case is not caused directly by the laser. Rather, a radiation driven "burn wave" propagates from front to back. Figure 41 shows the mesh radiative heat flux in erg/cm^2/s. The magnitude reaches approximately 50% of the incident laser heat flux. The spectrum of re-emission is centered at shorter wavelengths where the plasma is underdense, permitting transport of radiation into the bulk of the target. After the 2.5 ns required to burn through, the final temperature profile is homogenized as a result of strong radiation coupling throughout the target.

3.3 Decrease of thickness to 0.5 mm

After observing the strong absorption of the laser the front half of the target in the low-density (2 mg/cm^3) base case, we decided to examine a case that was tailored to allow all of the target to experience direct heating by the laser. We chose a case with 0.5 mm thickness, keeping all of the other parameters fixed.

Figure 42 shows the laser flux through each zone *vs.* time. Unlike the previous cases, the laser is clearly transmitted into the deepest parts of the target. The absorption is relatively uniform and relatively complete. The electron temperature, however, is **not** more uniform as compared with the base case. Figures 43 and 44 show that the magnitude of the electron temperature is roughly the same, but this case is slightly *less* uniform than the base case, and certainly less uniform than the high density case. It appears that optically thin laser absorption is less effective at homogenizing the temperature as compared with either a laser propagation wave or a radiation burn wave.

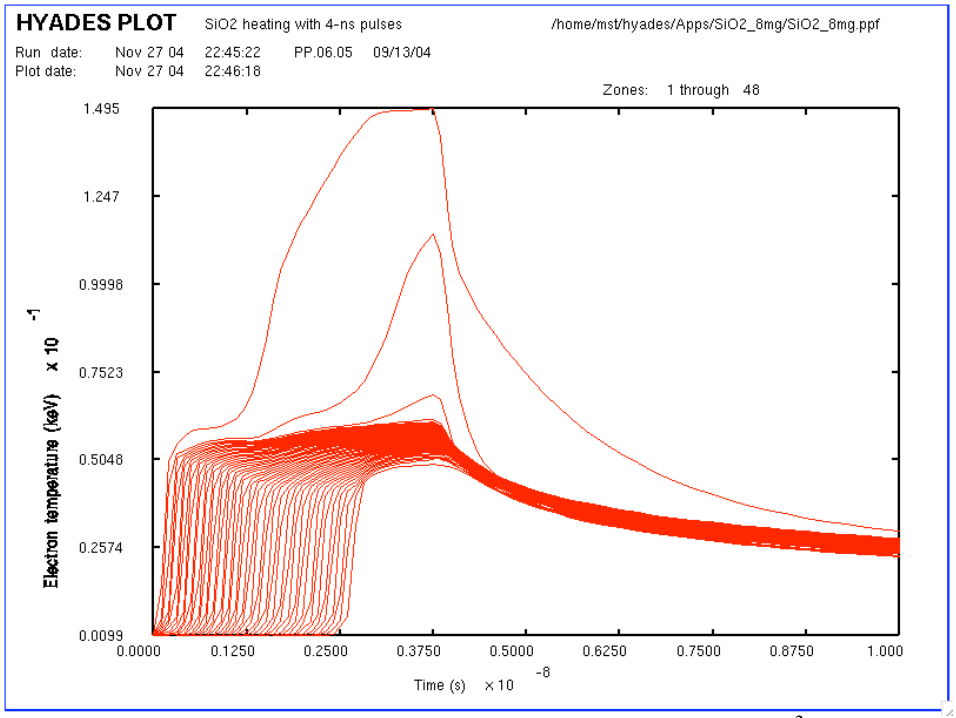

Figure 40. Electron temperature history for the 8 mg/cm^3 target

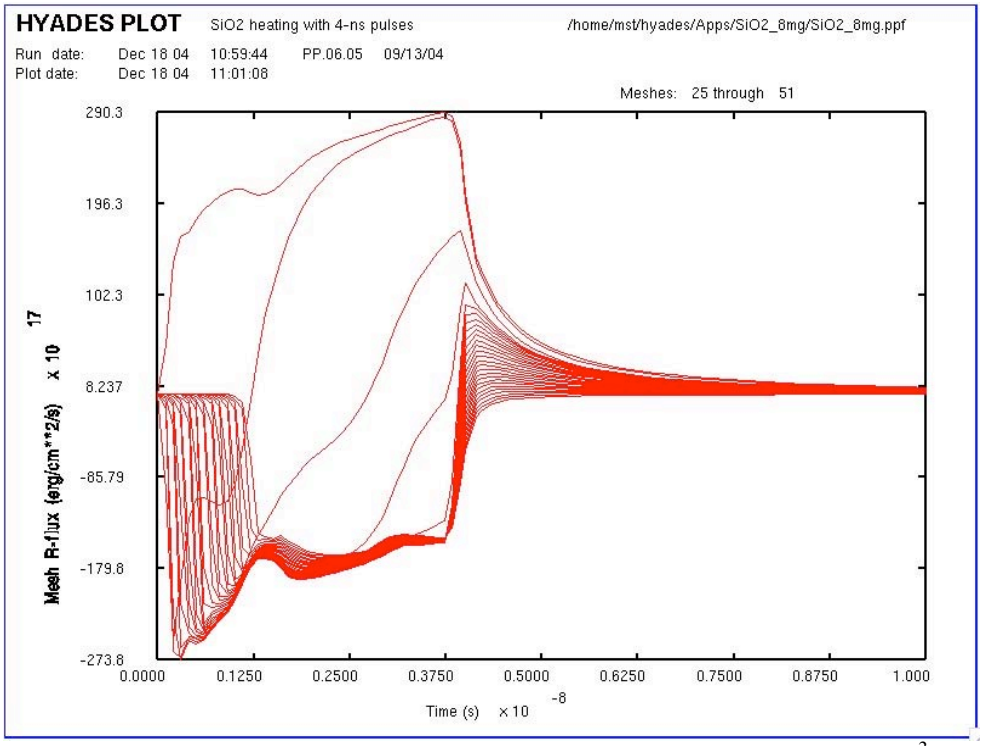

Figure 41. Mesh radiative heat flux as a function of time for the 8 mg/cm^3 target

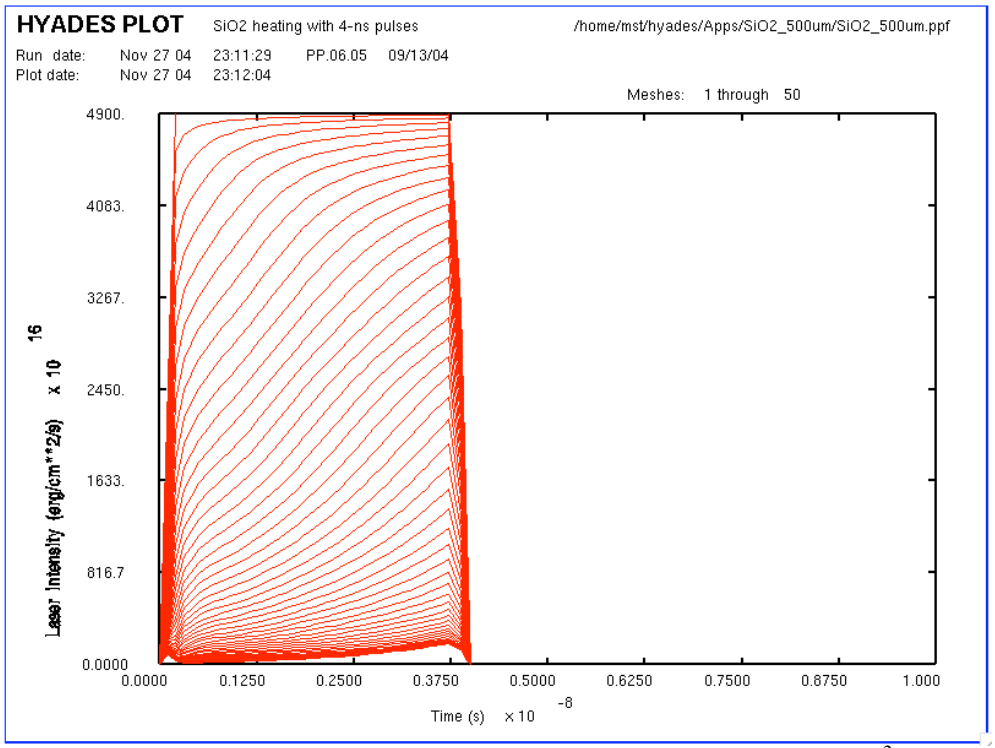

Figure 42. Time history of laser flux in the 0.5-mm thick, 2 mg/cm^3 target

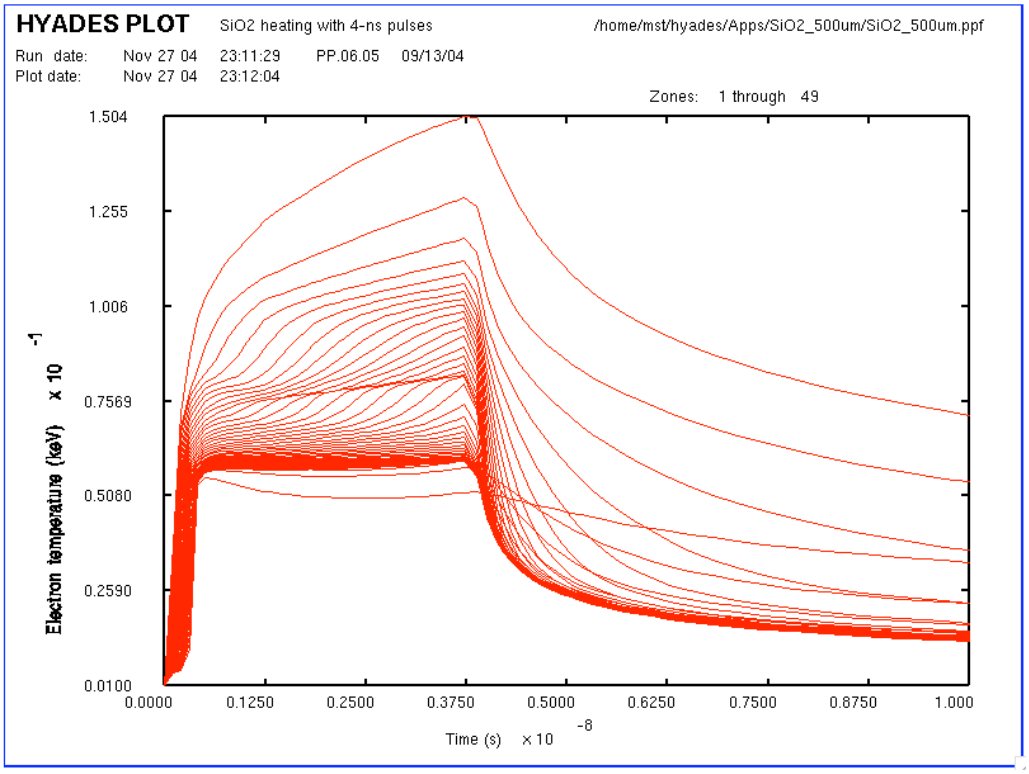

Figure 43. Electron temperature history for the 0.5-mm target

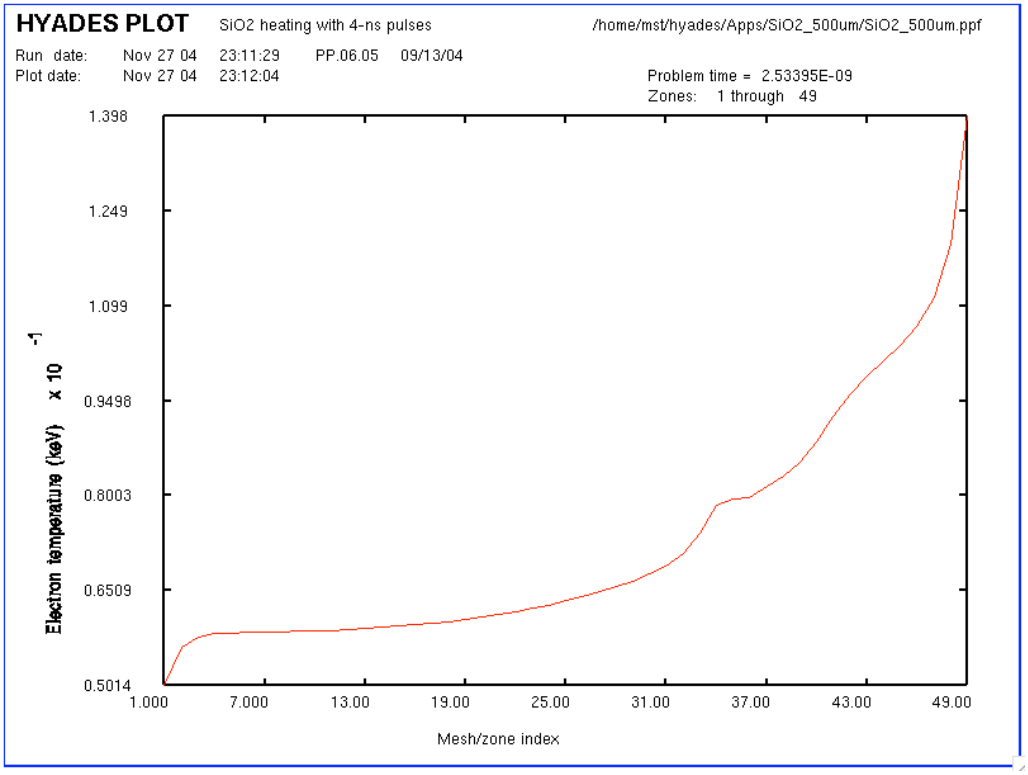

Figure 44. Electron temperature profile at 2.5 ns for the 0.5-mm target

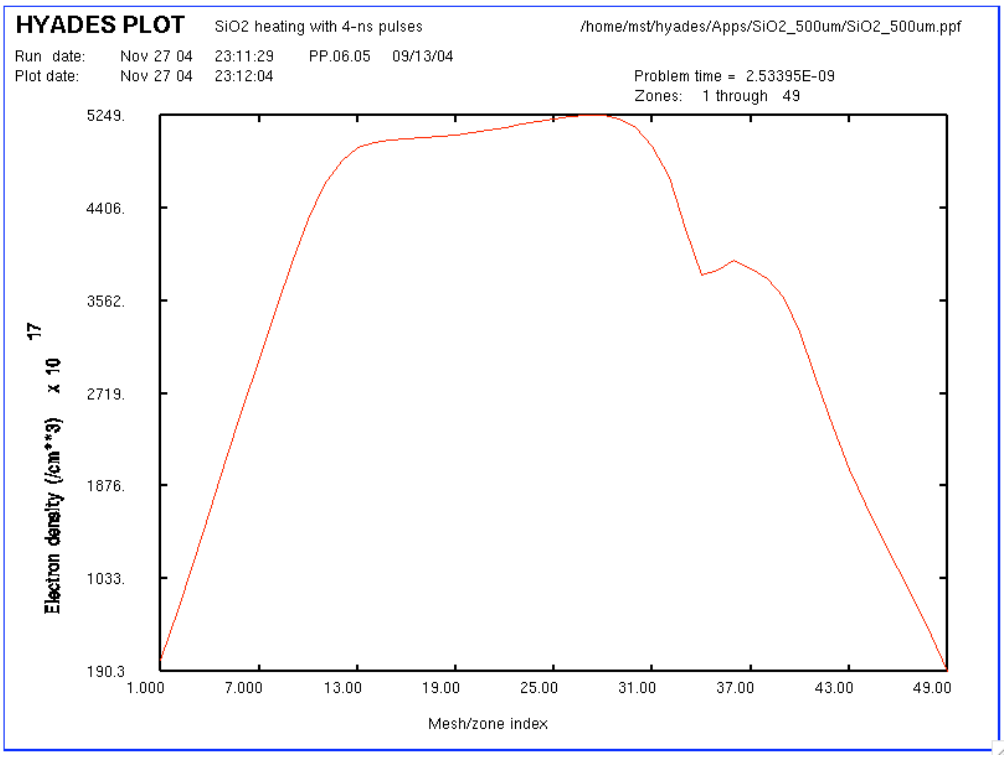

Figure 45. Electron density profile at 2.5 ns for the 0.5-mm target

Figure 45 shows the electron density profile at 2.5 ns for this case. The peak value is very similar to the other cases, but the hydrodynamically affected region appears somewhat larger. In fact, thee thickness of the hydrodynamically expanded region is similar to the base case, but appears larger in a relative sense due to the smaller target thickness. If a target that is transparent to the laser is desired, then a better strategy would be to reduce the density further – to about 1 mg/cm^3. However, the uniformity of the temperature is actually worse in this case, such that denser targets are probably more desirable.

3.4 Increase of laser intensity from 4.9x10^{12} W/cm^2 to 3.7x10^{14} W/cm^2

3.4.1 High intensity Hyades result

Laser intensities above 10^{14} W/cm^2 provide much stronger interactions as compared with those at 4.9x10^{12} W/cm^2. The stability of codes such as Hyades and Helios are tested under these conditions. Figures 46 and 47 show the evolution of electron temperature and density for this laser intensity, keeping all other parameters identical to the base case. These plots provide spatial profiles for time increments of 0.2 ns from 0 to 4 ns. Results after the laser is turned off were excluded; the profiles rapidly collapse and tend to obscure the results during the pulse. Both figures indicate fluctuations in the early stage of the laser pulse. We ran a case with a finer

grid and observed similar behavior, although at a different location in the plasma. We believe these fluctuations are numerical in origin, and not indicative of the real plasma response.

These high-intensity cases are characterized by more rapid heating, more uniform temperature profiles, and a rapid achievement of full ionization (see Figure 48). The peak temperature observed is approximately 1.5 keV.

Figure 49 shows the Lagrangian zone locations *vs.* time. The target explodes much more rapidly under this value of incident laser intensity. By the end of the pulse (see Figure 47), the peak electron density has dropped by a factor of 2, and the profile has become considerably nonuniform.

Figure 50 shows the laser flux within the target as a function of time. It is apparent that this target becomes optically thin toward the incident laser rather quickly. By the end of the laser ramp-up, the rear side already sees direct exposure, with ~30% of the incident laser flux passing through the target completely. By the end of the pulse, approximately 80% of the incident laser leaks through the target without absorption.

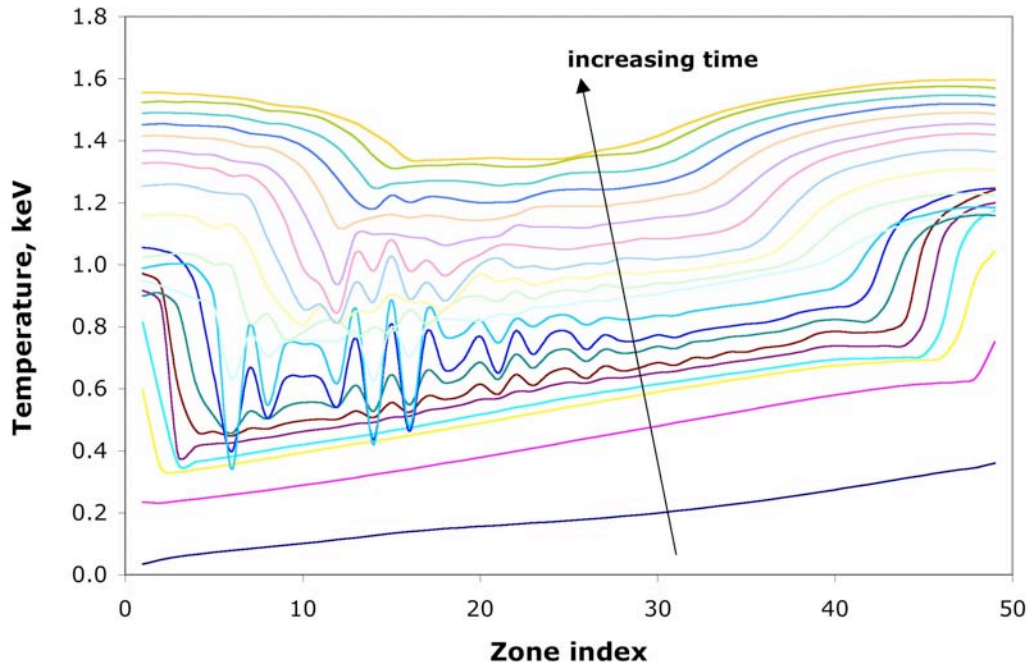

Figure 46. Electron temperature profiles at various times with 3.7×10^{14} W/cm^2 laser intensity

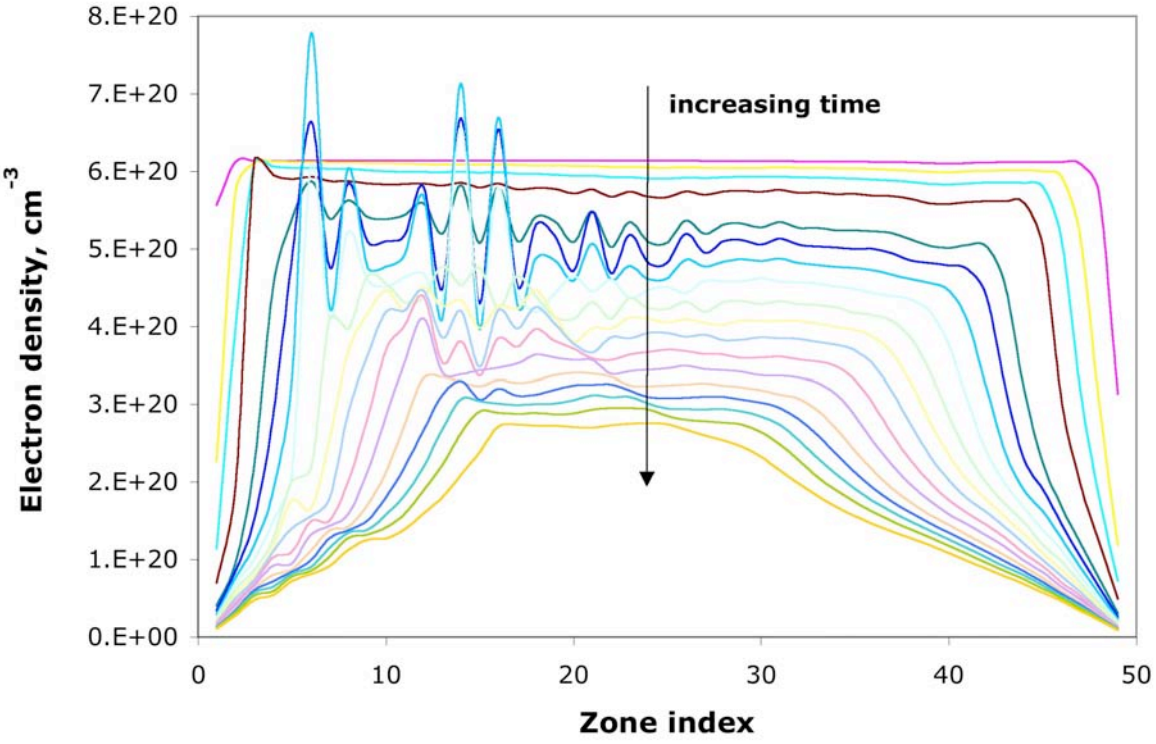

Figure 47. Electron density profiles at various times with 3.7×10^{14} W/cm^2 laser intensity

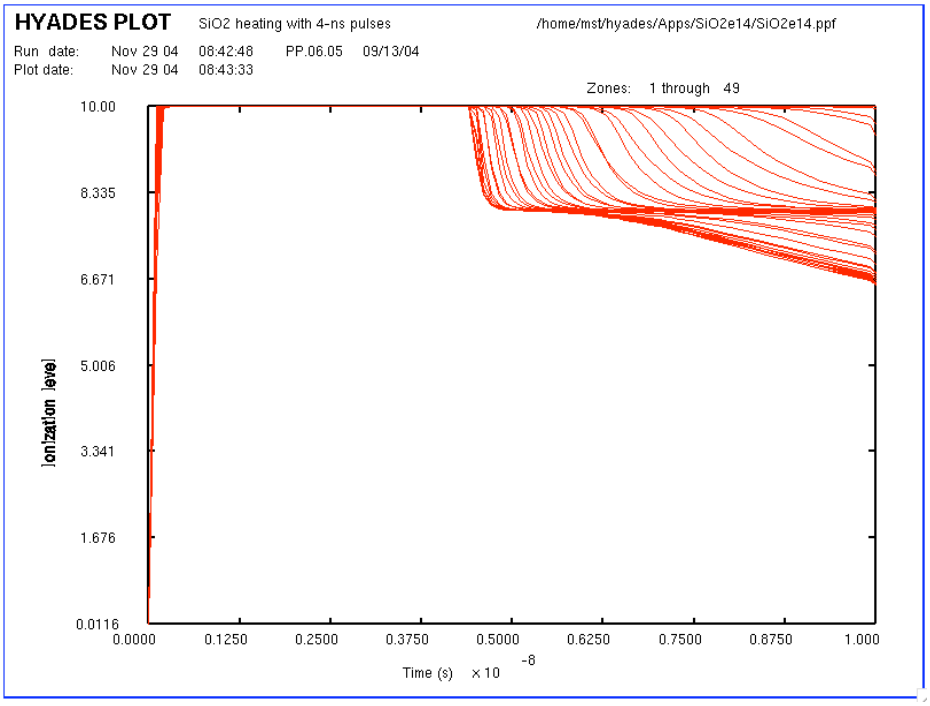

Figure 48. Time history of the charge state with 3.7×10^{14} W/cm^2 laser intensity

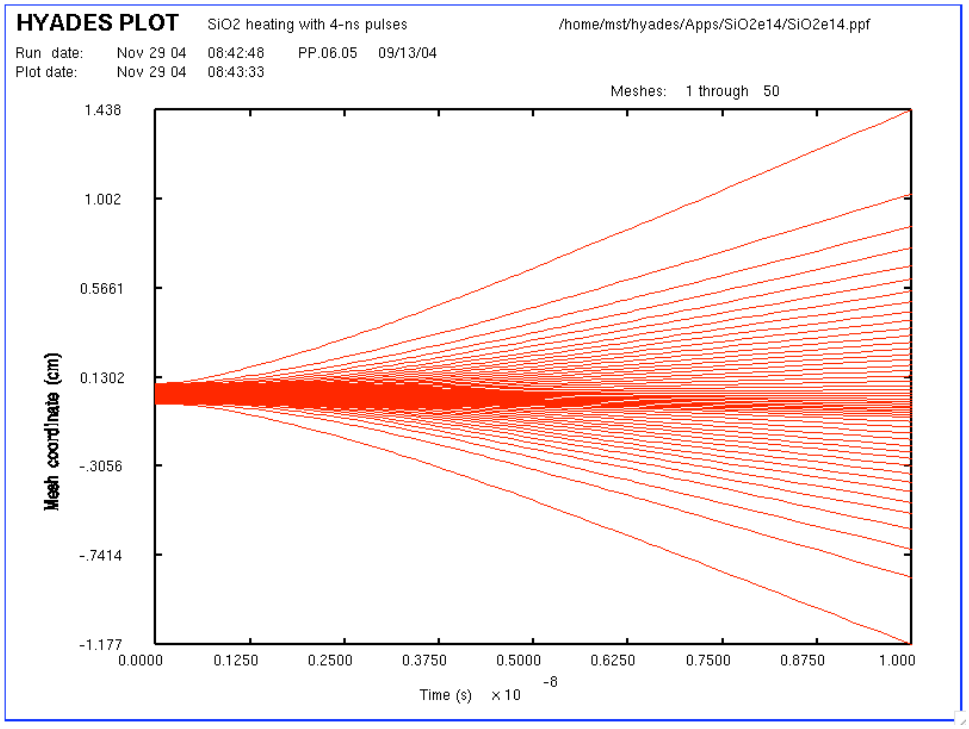

Figure 49. Radial location of the Lagrangian zones with 3.7×10^{14} W/cm^2 laser intensity

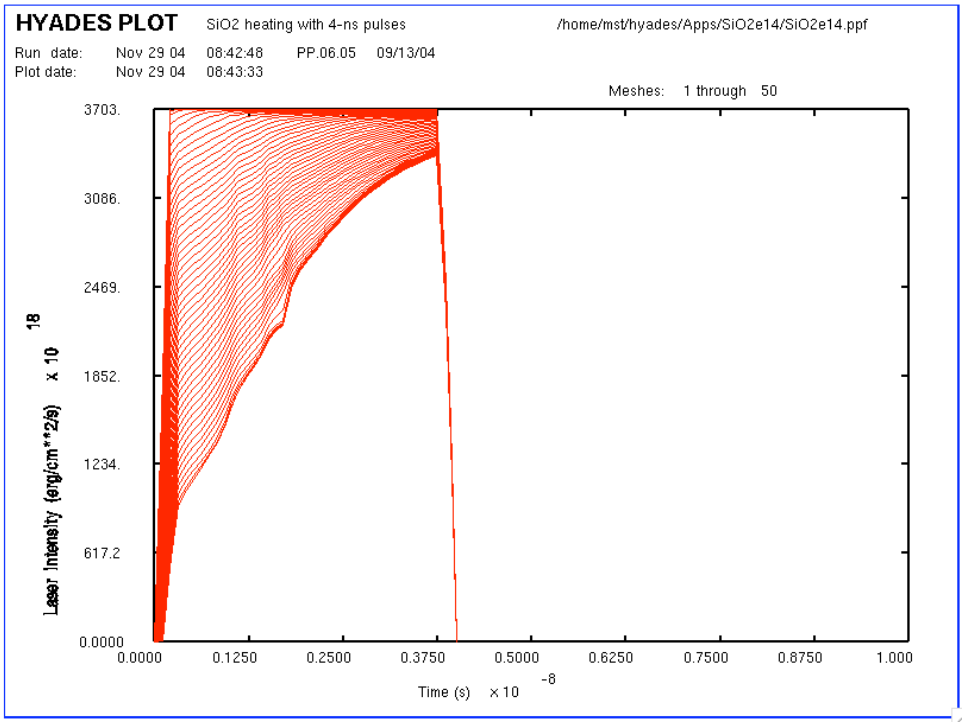

Figure 50. Time history of the laser flux with 3.7×10^{14} W/cm^2 laser intensity

3.4.2 High intensity Helios results, with and without doping

For the sake of comparison, we also explored the high intensity case using Helios. Figures 51–53 show the response for the target with 6% Ti doping. Figure 51 shows the electron temperature history, which can be compared with the Hyades high-intensity case (Figure 46). Similar to our earlier observations, Helios consistently predicts higher electron temperatures for the same conditions. The profiles are so flat that they can not be distinguished. Figure 52 shows a spatial profile at 2.5 ns. In order to explore the effect of doping at this elevated temperature, we also ran a case with no Ti. As seen in Figure 53, there is no distinuishable difference. This is not surprising; all of the atoms in this plasma are fully stripped, such that atomic processes are relatively unimportant during the laser pulse.

Figure 54 shows the electron density profile at 2.5 ns. The results are in general agreement with Hyades results, showing substantial hydrodynamic motion at this point in the laser pulse.

Based on the observation of the limited effect of dopant on the temperature evolution, we also explored the importance of spectral detail in the opacities. Figure 55 shows the result of this case. As the laser intensity is increased to 3.7×10^{14} W/cm^2 and successive atomic shells become stripped, it is expected that the *early time* electron temperature of these underdense plasmas will be relatively unaffected by a lack of spectral detail in the gray opacity data. As the plasma cools and recombines, atomic shells begin to repopulate. The radiation produced from *late time* processes depends upon specific spectral line properties such as excited state energy levels, atomic oscillator strengths, degeneracies, and ground state populations (for self-absorption considerations). To properly account for the intensity of line emission and associated absorption coefficient, spectral detail then becomes necessary.

Figure 55 shows that the peak electron temperature varies less than 20% between the gray and full spectral opacity runs. Rapid cooling is indicated in the early phase of the laser pulse, dropping the temperature from over 2 keV to approximately 1.5 keV.

In the late time recombination phase of the plasma, the emission begins to deviate significantly from a Planckian spectrum, resulting in an elevated electron temperature for the spectrally resolved case. This suggests that above a certain threshold temperature, spectral lines may become self-absorptive, resulting in trapped radiation that couples to thermal electrons.

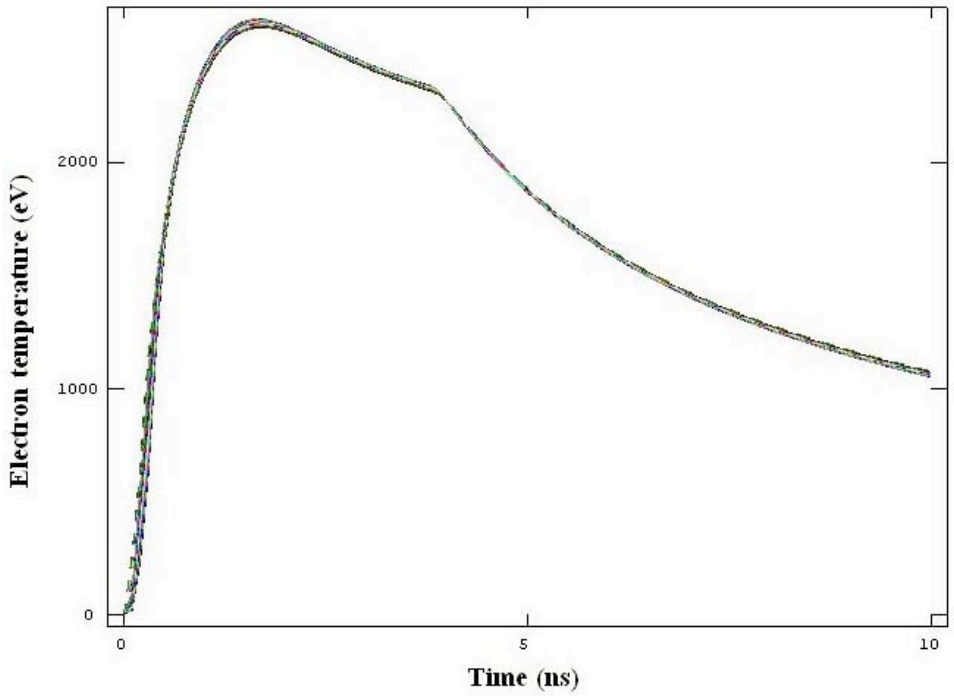

Figure 51. Electron temperature history for SiO_2-6% Ti using Helios

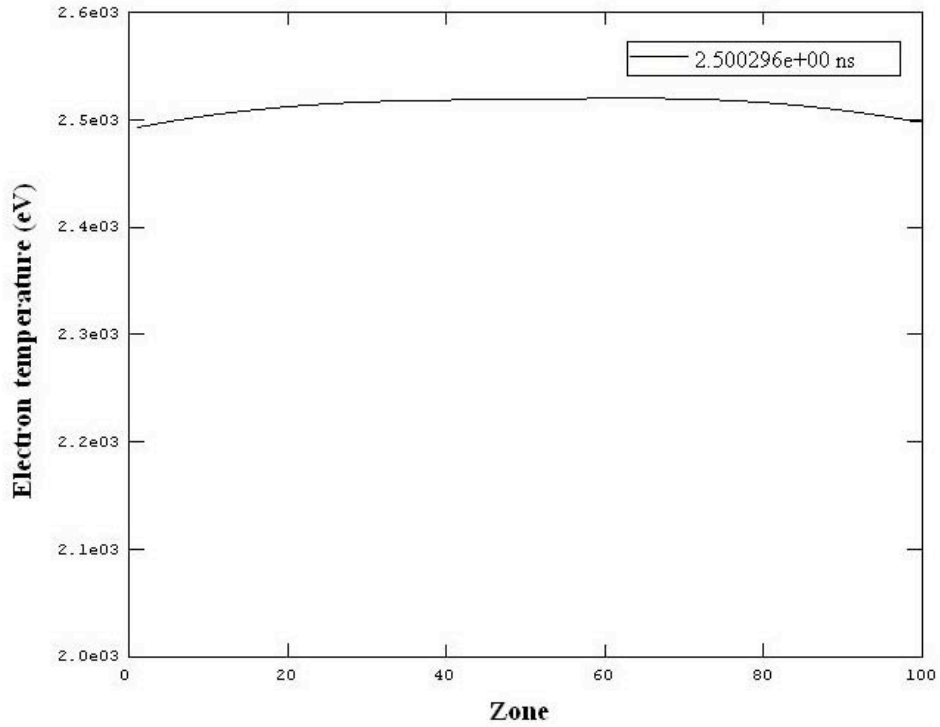

Figure 52. Electron temperature spatial profile at 2.5 ns for SiO_2-6% Ti using Helios

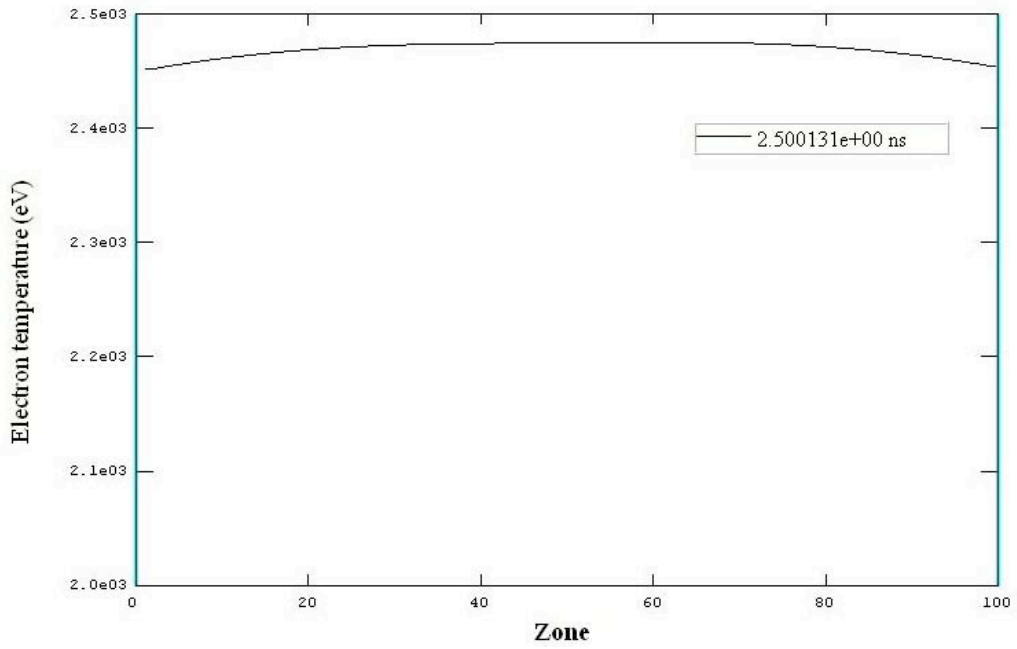

Figure 53. Electron temperature spatial profile at 2.5 ns for SiO_2-0% Ti using Helios

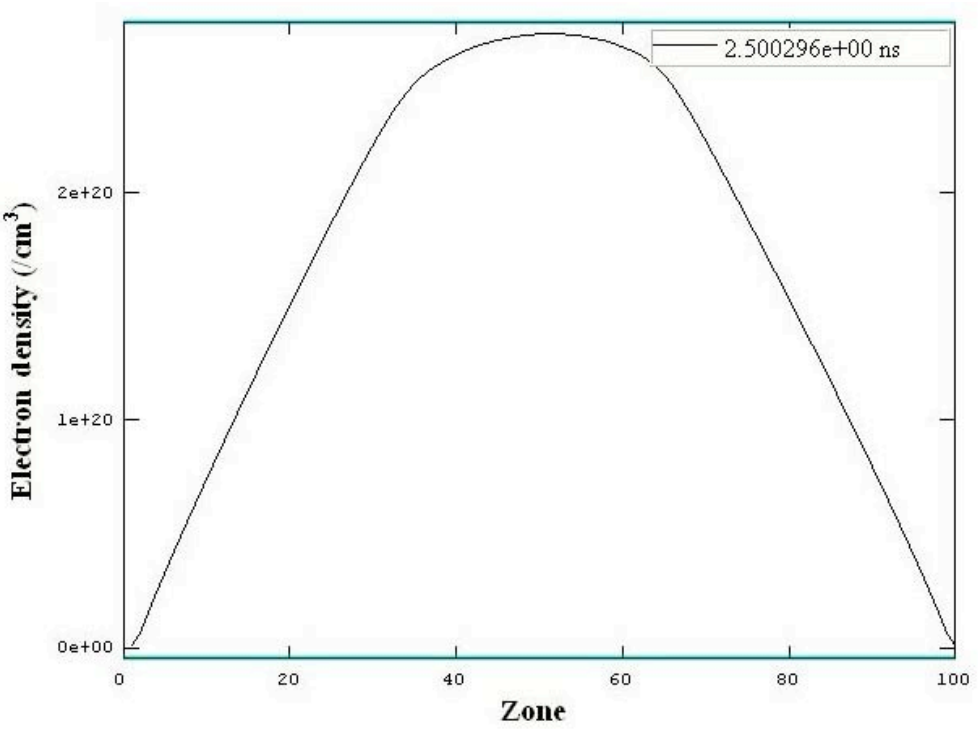

Figure 54. Electron density spatial profile at 2.5 ns for SiO_2-6% Ti using Helios

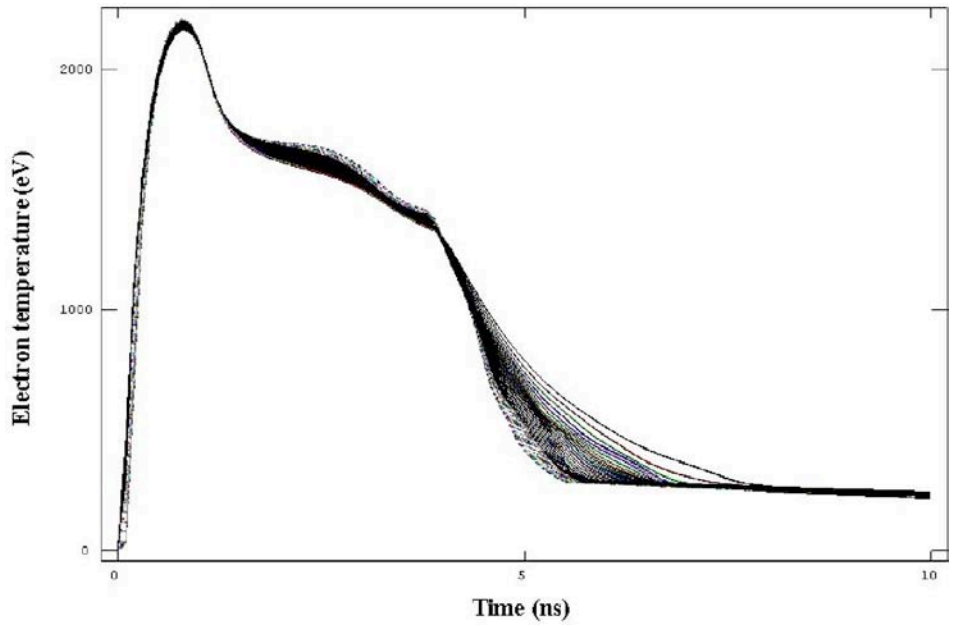

Figure 55. Electron temperature history for SiO_2-6% Ti using Helios with gray opacities

4. Summary and conclusions

We have examined the response of low-density SiO_2 aerogel targets to short pulse laser irradiation using the radiation hydrodynamic models Hyades and Helios. We explored the sensitivity of the results to changes in the models and data used, and then characterized the response over a range of parameters including Ti dopant concentration, target density, and laser intensity.

A "modeling base case" was explored in depth in order to understand the baseline behavior of a pure SiO_2 target exposed to the lower value of laser intensity. This study illuminated the basic behavior of the 2 mg/cm^2 underdense target. For this target, the laser "burns in" through a combination of a "laser absorption wave" and upconversion of energy to shorter wavelengths, which propagate more easily through the target. The rear of the target reaches a temperature of 50-100 eV (depending on the code used), and the front reaches 100-200 eV, with relatively strong gradients resulting from direct laser heating.

A laser propagation wave occurs in underdense plasmas as a result of the decrease in inverse bremsstrahlung absorption (which predominates in underdense cases) with heating. A radiation propagation wave occurs as a result of the upconversion of laser radiation into shorter wavelength atomic radiation. The optical depth generally decreases with increasing wavelength, and so the converted energy propagates more deeply as the front of the target becomes hotter.

In every case studied, the electron density achieves quite uniform values which are determined primarily by the ionization state of the target. At the lower intensity, the target becomes He-like (<Z>=8) and maintains a constant density until hydrodynamic expansion explodes the target.

This occurs near the end of the 4-ns laser pulse. At the higher intensity, the target is fully stripped (<Z>=10). Hydrodynamic expansion is far more rapid, and already results in a drop in density and very nonuniform profiles after 1 ns.

Targets with lower mass or mass density *do not* appear to heat more uniformly. The 8 mg/cm^3 case had the most uniform temperature, although it required more time for a radiation wave to penetrate. Laser absorption in this target was confined to a few nodes near the surface throughout the entire pulse. The 0.5-mm low-density case heated quickly, but did not lead to a more uniform temperature. Apparently plasmas heated indirectly are able to establish more uniform profiles than those heated directly by the incident laser.

Since the 2 mg/cm^2 target was not optically thin toward the laser at the lower intensity level, we explored a case with 0.5 mm thickness. Indeed, this target allowed light to penetrate fully into the target, but the smaller dimension also led to a substantial fraction of the mass being ejected by hydro motion before the entire target heats up. A better way to achieve optically thin targets would be to reduce the mass density. However, as mentioned above, this *is not* likely to lead to more uniform temperatures unless the target is so thin optically that the intensity does not vary substantially through the target.

The high intensity case behaved dramatically different than the base case. Due to rapid, complete ionization, this case became relatively insensitive to atomic processes. The temperature profile remained extremely flat throughout the laser pulse. The electron density has reasonably uniform profiles initially, but the hydrodynamic expansion is so extreme that the density drops almost immediately (after 1 ns) and becomes centrally peaked. At the same time, the plasma temperature gradually increases until the end of the pulse. By the time the plama reaches 1 keV (2 keV for Helios runs), the density profile is already significantly distorted.

Since radiation transport is one of the dominant mechanisms by which targets heat, cool and transport energy, treating the opacity, or absorption and re-radiation of photons is fundamental to determine the plasma evolution. We explored different opacity models and the effect of spectral resolution. In order to explore the effect of spectral detail in Hyades, we attempted to model multi-group radiation transport with the built-in model, and we attempted to import spectrally resolved PROPACEOS data. Unfortunately, neither of these efforts was successful.

Helios treats spectrally resolved opacities as an integral feature of the code. We analyzed cases with 1, 50, and 500 frequency groups. For the single-group case, the data are averaged using the Rosseland mean. The results in pure SiO_2 showed modest influence of spectral detail.

In order to explore the effect of dopant, we generated gray opacities for Hyades and we obtained data from Prism Compuational Sciences for SiO_2-2% Ti and SiO_2-6% Ti. Not unexpectedly, dopant had little influence on the target evolution in the case of gray opacities. Spectral averaging effectively smears out atomic processes. However, even in the case of spectrally resolved opacities used in Helios, still there was very minor influence of the dopant for the low-intensity case. For the high-intensity case, there is even less effect due to the complete ionization of the target.

Future modeling activities will focus on modeling of non-LTE processes and a closer examination of the target emissions after the laser pulse.

Acknowledgements

The authors would like to thank Jon Larsen at Cascade Applied Sciences, Joe MacFarlane, Igor Golovkin and Pam Woodruff at Prism Computational Sciences for advice and assistance in the use and interpretation of their software and data.

References

1. J. T. Larsen and S. M. Lane, "HYADES – A plasma hydrodynamics code for dense plasma studies," *J. Quant. Spectrosc. Radiat. Transfer,* **51** (1994) 179-186.

2. I. E. Golovkin, J. J. MacFarlane[1], P. R. Woodruff, L. A. Welser, D. L. McCrorey, R. C. Mancini, J. A. Koch, "Modeling of Indirect-Drive ICF Implosions using 1D Hydrodynamic Code with Inline Collisional-Radiative Atomic Kinetics," *Inertial Fusion Science and Applications 2003*, Monterey CA, Sept. 2003 (pp. 166-169).
(see also http://www.prism-cs.com)

3. P. G. Burkhalter, M. J. Herbst, D. Duston, J. Gardner, M. Emery, R. R. Whitlock, J. Grun, J. P. Apruzese, and J. Davis, "Density and temperature profiles within laser-produced plasmas in the classical-transport regime," *Phys. Fluids* **26**, 3650-3659 (1983).

4. NLTE Code Comparisons Workshop reports, 1996 and 1998.

5. S. P. Lyon and J. D. Johnson (Eds.), "SESAME, the Los Alamos National Laboratory equation of state database," Los Alamos National Laboratory report LA-UR-92-3407 (1992).
(see also http://t1web.lanl.gov/newweb_dir/t1sesame.html)

6. J. Denavit and D.W. Phillion, "Laser ionization and heating of gas targets for long-scale-length instability experiments," *Phys. Plasmas* **1**, 1971 (1994).

7. R. Siegel and J. R. Howell, Thermal Radiation Heat Transfer, Hemisphere Publishing Corporation, 1992.

Appendices

Appendix A. Original Statement of Work

Proposal for Collaboration on EUV/XUV experiments and modeling

Mark S. Tillack

Mechanical and Aerospace Engineering Department
University of California, San Diego
11 June 2004

We propose to collaborate with LLNL on spectroscopy experiments and analysis related to x-ray emission in the EUV and XUV range from laser-produced plasmas. This work is in support of experiments in progress at the Nike and Janus laser facilities. Members of the fusion energy group at the University of California San Diego will run simulations and help analyze data as specified by LLNL personnel.

The following five elements are proposed for the scope of work:

1. Using the hydrodynamics code Hyades, provide analysis and predictions of the plasma conditions attained by Ti-aerogel in Nike and Janus laser experiments. This will include license fees for Hyades.

2. Support a graduate student to run calculations with Hyades and Cretin.

3. Evaluate the use of different atomic models for the simulations of the experiments.

4. Travel for discussions on results and future plans.
   – 1 week total to be split between LLNL and UCSD locations

5. Develop a detailed plan for continued collaboration and student support. This includes identifying appropriate experimental or theoretical themes of research relevant to the development of absolute spectroscopic diagnostics.

Appendix B. Input and source files

Appendix B.1 Hyades input file for the base case

```
SiO2 heating with 4-ns pulses
c
c 1 mm (.1 cm) slab of SiO2 with 50 nodes, NO feathering
c
mesh 1 51  0.00 0.1 1.0
c
c fully dense glass is 2.6 g/cc
c this run uses 0.1% dense SiO2 (2.04e-3 g/cc)
c and initial electron temperature of 1 eV
c
region  1 51 1 2.04e-3 0.001
c
c Z=10, A=20
c EOS for silica is 24
c opacity of quartz is 1022
c
material 1 10. 20. 1.
eos   24 1
eos 1022 1
c
c 4.9e+12 watts/cm**2 (10^21 erg/cm2/s), 0.248 um laser source
c rises in 5 fs, flat-topped for 10 fs
c
source laser 0.248 -51
tv 0. 0.
tv 0.2e-9 4.9e+19
tv 3.8e-9 4.9e+19
tv 4.0e-9 0.
c
pparray r dene te tr deplas qrad u zbar xmass acc xlsint
c
c use 0.1 ns output time intervals initially, stop after 1 ns
c
parm postdt 1.e-10
parm tstop 1.e-8
c
```

Appendix B.2 Source listing for spectral averaging routine

```
implicit double precision (a-h,o-z)
      character*120 header
      character*15 filename
      character*1 tab
      dimension d(100), t(100), e(10000), a(10000)
      dimension ross(100,100), plan(100,100), opacr(100), opacp(100)
      external rossave, planckave, planck, planckd

      tab = "\t"

      open(unit=5, file="SiO2.dat", recl=132)
      open(unit=6, file="averages", status="unknown")

      read(5,*) nt                    ! number of temperatures
      read(5,*) (t(i),i=1,nt)         ! temperatures
      read(5,*) nd                    ! number of densities
      read(5,*) (d(i),i=1,nd)         ! densities
      read(5,*) ng                    ! number of energy groups
      read(5,*) (e(i), i=1,ng+1)      ! energies

      write(6,*) "Planck and Rosseland Averages"

      do id=1,nd
      do it=1,nt
        temp = t(it) * 11604.4

        read(5,2) header
        read(5,*) (a(n), n=1,ng)   ! Rosseland opacity

        read(5,2) header
        read(5,*) (a(n), n=1,ng)   ! Planck emission opacity

        read(5,2) header
        read(5,*) (a(n), n=1,ng)   ! Planck absorption opacity

c place these two statements after the appropriate read statement
        plan(it,id) = planckave(a,e,temp,ng)
        ross(it,id) = rossave(a,e,temp,ng)
c -------------------------------------------------------------

      enddo
      enddo

    1 format(2x,10(2x,e12.4))
    2 format(a120)

c at this point the data has been entered and averages done.
c next, we want to interpolate opacity vs. T at n=5x10^20/cm3

      write(6,*) "opacity vs. temperature at n=5x10^20"

      dout = 5.e20
```

```
      ir = 1
      do while (dout .gt. d(ir))
        ir = ir + 1
        if(ir.gt.nd) then
          write(*,*) "desired density outside range"
          stop
          endif
        enddo

c ir is the index where the density data point exceeds 5e20
c frac=1 at dout=d(ir)
      frac = (dout-d(ir-1))/(d(ir)-d(ir-1))
      write(6,*) "ir=",ir
      write(6,*) "frac=",frac

c interpolate the opacity vs. temperature and write to output file
      do io = 1, nt
        opacr(io) = frac*ross(io,ir) + (1.-frac)*ross(io,ir)
        opacp(io) = frac*plan(io,ir) + (1.-frac)*plan(io,ir)
        write(6,5) t(io), tab, opacp(io), tab, opacr(io)
        enddo

    3 format(e12.4,a1,e12.4)
    5 format(e12.4,a1,e12.4,a1,e12.4)
      stop
      end

c *******************************************************
c Perform the Rosseland integration
      function rossave(a,e,temp,ngroup)
      implicit double precision (a-h,o-z)
      dimension e(10000), a(10000)

      top = 0.
      denom = 0.

      do i=1,ngroup
        de = e(i+1)-e(i)
        eave = 0.5*(e(i+1)+e(i))
        xl = 1.24/eave            ! wavelength in microns
        pl = planckd(temp,xl)
        top = top + de * pl / a(i)
        denom = denom + de * pl
        enddo
      rossave = denom/top

      return
      end

c *******************************************************
c Perform the Planck integration
      function planckave(a,e,temp,ngroup)
      implicit double precision (a-h,o-z)
      dimension e(10000), a(10000)

      top = 0.
```

```
      denom = 0.
      do i=1,ngroup
        de = e(i+1)-e(i)
        eave = 0.5*(e(i+1)+e(i))
        xl = 1.24/eave            ! wavelength in microns
        pl = planck(temp,xl)
        top = top + a(i) * pl * de
        denom = denom + pl * de
        enddo

      planckave = top/denom
      return
      end

c ********************************************************
c Evaluate the Planck function at T
      function planck(t,xl)
      implicit double precision (a-h,o-z)
      data c1, c2, pi / 5.9555e7, 1.4388e4, 3.1415926 /
      planck = 2.*pi*c1/xl**5/(exp(c2/xl/t)-1.)
      return
      end

c ********************************************************
c Evaluate the Planck derivative at T
      function planckd(t,xl)
      implicit double precision (a-h,o-z)
      data c1, c2, pi / 5.9555e7, 1.4388e4, 3.1415926 /

c we evaluate this by differencing because the function
c itself is ill-behaved

      t2=t*1.001
      p1 = planck(t,xl)
      p2 = planck(t2,xl)
      planckd = (p2-p1)/(t2-t)
      return
      end
```

Appendix B.3 Source listing for Sesame mixture generator

```
c This routine creates Hyades EOS and opacity files for mixtures
c using a mass-weighted arithmetic average of the two input datasets.
c We assume here that the mixture plasma has a single state (n,T),
c and that the eos and opacity of the constituents are evaluated at
c the mixture (n,T).  The values of (n,T) in the output are chosen
c to match those of the primary constituent (file 1).  Interpolation
c on (n,T) is used to add a fraction of the second dataset.  The (n,T)
c ranges are truncated if the data range of the second constituent
c is smaller than the first.  This avoids extrapolation outside the
c database for either constituent.

c INPUT FILE PARAMETERS (eosmix.dat)
c header    = output file header line
c numeos    = a unique eos numeric identifier for the mixture
c filename1 = first input file
c filename2 = second input file
c filename3 = output file name
c wtp       = mass fraction of the second constituent (2nd file)

c Sesame file format:
c line 1 -- header
c line 2 -- property identifier, Zbar, Abar, rho, npts
c        (where npts is the remaining number of variables in the file)
c line 3 -- number of density values, number of temperature values,
c           density array, temperature array, first property array,
c           second property array

c for opacities, properties are Rosseland and Planck opacities
c for EOS it's pressures and energies

c the order of indexing in the parameter arrays is to scan densities
c first -- i.e., p(nd,nt) scans through nd points, nt times

c p1f1 - first property in first input file
c p2f1 - second property in first input file
c p1f2 - first property in second input file
c p2f2 - second property in second input file
c p1f2i - first property in second input file, interpolated
c p2f2i - second property in second input file, interpolated
c p1f3 - first property in output file
c p2f3 - second property in output file

c -------------------
c -- BEGIN PROGRAM --
c -------------------
      character*80 header, dummy
      character*12 filename1, filename2, filename3
      real*4 array1(10000), array2(10000), array3(10000)
      real*4 d1(100), t1(100), d2(100), t2(100)
      real*4 p1f1(100,100), p2f1(100,100), p1f2(100,100), p2f2(100,100)
      real*4 p1f2i(100,100),p2f2i(100,100),p1f3(100,100), p2f3(100,100)

      external xmaxval, pack, unpack
```

```
c read the user supplied parameters
      open (unit=5,file='eosmix.dat')
      read(5,*) header
      read(5,*) numeos, filename1, filename2, filename3, wtp
      close(5)

c read the first dataset
      open(unit=5, file=filename1)
      read(5,*) dummy
      read(5,*) nonum, zbar1, abar1, rho1, n1
      read(5,*) (array1(i), i=1,n1)
      close(5)

c read the second dataset
      open(unit=5, file=filename2)
      read(5,*) dummy
      read(5,*) nonum, zbar2, abar2, rho2, n2
      read(5,*) (array2(i), i=1,n2)
      close(5)

c evaluate zbar, abar and rho
      zbar3 = (1.-wtp)*zbar1 + wtp*zbar2
      abar3 = (1.-wtp)*abar1 + wtp*abar2
      rho3  = (1.-wtp)*rho1  + wtp*rho2

c ------------------------------------------------------------
c move input 1-d arrays into p1(nd,nt) and p2(nd,nt) 2-d arrays
c   * for opacities, this is Rosseland and Planck opacities
c   * for EOS it's pressures and energies
c ------------------------------------------------------------

c unpack first array
      call unpack(array1,d1,t1,p1f1,p2f1,nd1,nt1,incr)

c check incr=n1 at this point, otherwise STOP
      if(incr.ne.n1)then
        open(unit=8, file='test.dat')
        write(8,*) 'STOP at increment check n1'
        stop
        endif

c unpack second array
      call unpack(array2,d2,t2,p1f2,p2f2,nd2,nt2,incr)

c check incr=n2 at this point, otherwise STOP
      if(incr.ne.n2)then
        open(unit=8, file='test.dat')
        write(8,*) 'STOP at increment check n2'
        stop
        endif

c ------------------------------
c Establish the output array size
c ------------------------------
```

```
c find the maximum values of n and T in file 2
      dmax2 = xmaxval(d2,nd2)
      tmax2 = xmaxval(t2,nt2)

c truncate the arrays, if needed:
c   find the largest value of (d1,t1) which are smaller than (d2,t2)
      i=nd1
      do while(d1(i).gt.dmax2)
        i=i-1
        enddo
      nd1 = i

      i=nt1
      do while(t1(i).gt.tmax2)
        i=i-1
        enddo
      nt1 = i

c the new maximum values of d1 and t1:
      dmax1 = d1(nd1)
      tmax1 = t1(nt1)

c -----------
c Interpolate
c -----------
c we need to evaluate the second data set at the (n,T)
c values of the first data set (by linear interpolation)
c (n,T) increments:  (i,j) for first file, (m,n) for second

c It is assumed that d1(1)=d2(1) and t1(1)=t2(1)
c If not, then stop
      res = 1.e-6
      dcheck=abs(d1(1)-d2(1))/(d1(1)+d2(1))
      tcheck=abs(t1(1)-t2(1))/(t1(1)+t2(1))
      if(dcheck.gt.res) then
        open(unit=8, file='test.dat')
        write(8,*) 'STOP at d1(1)=d2(1)'
        stop
        endif
      if(tcheck.gt.res) then
        open(unit=8, file='test.dat')
        write(8,*) 'STOP at t1(1)=t2(1)'
        stop
        endif

c for each j of the first array we need the n point where Tn>Tj
      do j=1,nt1
        n=2
        do while (n.le.nt1 .and. t2(n).le.t1(j))
          n=n+1
          enddo
        gp = (t1(j)-t2(n-1))/(t2(n)-t2(n-1))
        gm = 1.-gp

c for each i of the first array we need the m point where dm>di
      do i=1,nd1
```

```
        m=2
        do while (m.le.nd1 .and. d2(m).le.d1(i))
          m=m+1
          enddo
        fp = (d1(i)-d2(m-1))/(d2(m)-d2(m-1))
        fm = 1.-fp

c now form the linear combinations
        p1f2i(i,j) = fp * gp * p1f2(m,n)
     .             + fp * gm * p1f2(m,n-1)
     .             + fm * gm * p1f2(m-1,n-1)
     .             + fm * gp * p1f2(m-1,n)
        p2f2i(i,j) = fp * gp * p2f2(m,n)
     .             + fp * gm * p2f2(m,n-1)
     .             + fm * gm * p2f2(m-1,n-1)
     .             + fm * gp * p2f2(m-1,n)
        enddo
        enddo


c now that we have the interpolated arrays, we simply
c weight the two datasets to form the output
      do j=1,nt1
      do i=1,nd1
        p1f3(i,j) = (1.-wtp)*p1f1(i,j) + wtp*p1f2i(i,j)
        p2f3(i,j) = (1.-wtp)*p2f1(i,j) + wtp*p2f2i(i,j)
        enddo
        enddo

c -----------------------------------------------------
c pack the output linear array for writing to the file
c -----------------------------------------------------

      call pack(array3,d1,t1,p1f3,p2f3,nd1,nt1,incr)

c check incr=n3 at this point, otherwise STOP
      n3  = 2 + nd1 + nt1 + 2*(nd1*nt1)
      if(incr.ne.n3)then
        open(unit=8, file='test.dat')
        write(8,*) 'STOP at increment check n3'
        write(8,*) 'incr=',incr,', n3=',n3
        stop
        endif

c ------
c OUTPUT
c ------
      open(unit=7, file=filename3)
      write(7,*) header
      write(7,1) numeos, zbar3, abar3, rho3, n3
      write(7,2) (array3(i), i=1,n3)
      close(7)

    1 format(1x,i5,4x,1p3e15.8,3x,i5)
    2 format(1p5e15.8)
```

```
      stop
      end

c *******************************************************
c EXTERNAL FUNCTION XMAXVAL
      function xmaxval(a,na)
      real*4 a(100)
      xmaxval=0.
      do i=1,na
        if(a(i).gt.xmaxval) xmaxval=a(i)
        enddo
      return
      end

c *******************************************************
c UNPACK a linear array into d(nd), t(nt), p1(i,j), p2(i,j)
      subroutine unpack(a,d,t,p1,p2,nd,nt,incr)
      real*4 a(10000), d(100), t(100), p1(100,100), p2(100,100)

c (0.01 is to avoid roundoff errors in integers)
      nd = aint(a(1)+0.01)
      nt = aint(a(2)+0.01)
      incr = 2

      do i=1,nd
        incr=incr+1
        d(i) = a(incr)
        enddo
       do i=1,nt
        incr=incr+1
        t(i) = a(incr)
        enddo

      do j=1,nt
      do i=1,nd
        incr=incr+1
        p1(i,j) = a(incr)
        enddo
        enddo
      do j=1,nt
      do i=1,nd
        incr=incr+1
        p2(i,j) = a(incr)
        enddo
        enddo
      return
      end


c *******************************************************
c PACK 2d arrays d(nd), t(nt), p1(i,j), p2(i,j) into a
      subroutine pack(a,d,t,p1,p2,nd,nt,incr)
      real*4 a(10000), d(100), t(100), p1(100,100), p2(100,100)

      a(1) = nd
      a(2) = nt
```

```
incr = 2

do i=1,nd
  incr=incr+1
  a(incr) = d(i)
  enddo
 do i=1,nt
  incr=incr+1
  a(incr) = t(i)
  enddo

do j=1,nt
do i=1,nd
  incr=incr+1
  a(incr) = p1(i,j)
  enddo
  enddo
do j=1,nt
do i=1,nd
  incr=incr+1
  a(incr) = p2(i,j)
  enddo
  enddo
return
end
```